Spin Torque and Spin Hall Nano-Oscillators with Single Magnetic Layers

Spin Torque and Spin Hall Nano-Oscillators with Single Magnetic Layers

Philipp Dürrenfeld

UNIVERSITY OF GOTHENBURG

Doctoral Dissertation in Physics

Department of Physics
University of Gothenburg
412 96 Göteborg, Sweden

June 2, 2015

ISBN: 978-91-628-9443-6 (printed)
ISBN: 978-91-628-9444-3 (pdf)
URL: http://hdl.handle.net/2077/38714

Cover: Top: Schematic of a spin Hall nano-oscillator containing a circular mesa and sharp-tip gold electrodes injecting a current into a nm-sized region of the NiFe/Pt bilayer. Bottom: SEM micrograph of a spin Hall nano-oscillator picturing the current and field directions necessary for auto-oscillations.

Printed by Kompendiet, Göteborg, 2015

Typeset using LuaLaTeX

Abstract

Spin-torque oscillators (STOs) are capable of producing tunable broadband high-frequency signals within a nanometer-sized region. In this thesis, novel designs for STOs will be discussed; the common theme of these designs will be their use of only one ferromagnetic (FM) material. This work was motivated by the need to understand the fundamental magnetization dynamics in such devices, improving signal quality, and reducing the complexities of device fabrication in comparison to conventional nanocontact (NC-)STOs based on a multilayered spin-valve structure.

Single-layer NC-STOs: The multilayered spin-valve structure in NC-STOs may be replaced by a material stack with a single FM layer, reducing the number of metallic layers as well as the total thickness of the devices. Spin-transfer torque (STT) can be efficiently created at the interface to the FM layer underneath the nanocontact, leading to the production of microwave signals in zero applied field.

Spin Hall effect (SHE) driven dynamics: A charge current flowing through platinum establishes spin accumulation at the edges of the material due to the SHE. This can be used for STT-driven magnetization dynamics in an adjacent FM layer. These so-called spin Hall nano-oscillators (SHNOs) operate with the current flow being directed in-plane, simplifying nanofabrication and allowing for direct optical access to the active area. SHNO devices are designed in two device geometries: One uses pointed gold electrodes to inject current into an extended active area, while the other focuses the current at a nanoconstriction.

Implementation of Heusler alloys: The magnetodynamics of STOs are governed by the properties of the FM free layer. The ease of fabrication of single-layer NC-STOs and SHNOs opens up the possibility of implementing nonconventional ferromagnets with unique magnetic properties. One such material is the epitaxially grown half-metallic half-Heusler alloy NiMnSb, which has a fundamentally lower magnetic damping than permalloy, leading to microwave emission spectra with ultralow linewidths.

Mutual synchronization of SHNOs: The mutual synchronization of STOs is accompanied by an increase in the output power and a decrease in the linewidth, thereby drastically improving the overall quality of the microwave signal. Here, the mutual synchronization of up to nine serially connected nanoconstriction SHNOs is demonstrated, which potentially opens up the possibility of implementing these devices in, for example, spin-wave-based computing.

Contents

List of Figures

List of Symbols and Abbreviations

List of Symbols

α	Gilbert damping constant
ΔH	linewidth (FWHM)
ΔH_0	inhomogeneous linewidth broadening
θ, θ_{ext}	out-of-plane angle of the external field
θ_{int}	out-of-plane angle of the magnetization
θ_{lin}	linear internal magnetization angle
Θ_{SH}	spin Hall angle
$\rho_{\parallel}$	resistivity for current parallel to magnetization
$\rho_{\perp}$	resistivity for current perpendicular to magnetization
σ^c_{xx}	longitudinal charge conductivity
σ^s_{xy}	transverse Hall conductivity
τ	spin-torque coefficient
φ	in-plane angle of the external field
A	exchange stiffness
$\vec{B}$,B	magnetic flux
d, d_{NM}, d_{FM}	layer thickness
d_{cc}	distance between two constrictions
f_0	ferromagnetic resonance frequency
f_{rf}	(external) microwave frequency
$\vec{H}_{eff}$	effective magnetic field
H, H_{ext}	external magnetic field
H_0	ferromagnetic resonance field
H_{ex}	exchange field
H_{int}	internal magnetic field
H_{Oe}	Oersted field
h_{rf}	microwave magnetic field
I	current
I_{beam}	ion beam current
$J_{C,rf}$	microwave charge current density
$J_{S,rf}$	microwave spin-current density
$\vec{k}$	wave vector
$\vec{M}$	magnetization
M_0	saturation magnetization

List of Symbols (continued)

M_{eff}	effective magnetization
N	nonlinear frequency coefficient
p	PSSW mode quantization number
$\vec{P}$	polarization of the spin/charge current
t	time
U_{acc}	ion beam acceleration voltage
U_{beam}	ion beam voltage
V_{mix}	mixing voltage

List of Physical Constants

$\gamma/(2\pi)$	gyromagnetic ratio of an electron	$28.024\,\mathrm{GHz/T}$
μ_0	vacuum permeability	$4\pi \times 10^{-7}\,\mathrm{V\,s/(A\,m)}$
μ_B	Bohr magneton	$9.274 \times 10^{-24}\,\mathrm{J/T}$
e	elementary charge	$1.602 \times 10^{-19}\,\mathrm{C}$
$\hbar$	reduced Planck constant	$1.055 \times 10^{-34}\,\mathrm{J\,s}$

List of Abbreviations

μ-BLS	microfocused Brillouin light scattering
ac	alternating current
AHE	anomalous Hall effect
AMR	anisotropic magnetoresistance
dc	direct current
CPW	coplanar waveguide
DUT	device under test
EBL	electron beam lithography
FM	ferromagnet, ferromagnetic
FMR	ferromagnetic resonance
FWHM	full width at half maximum
GGG	gadolinium gallium garnet ($Gd_3Ga_5O_{12}$)
GMR	giant magnetoresistance
HV	high vacuum
IBE	ion beam etching
LLGS	Landau–Lifshitz–Gilbert–Slonczewski (equation)
LNA	low noise amplifier
MBE	molecular beam epitaxy
MTJ	magnetic tunnel junction
NC	nanocontact
NC-STO	nanocontact spin-torque oscillator
NM	nonmagnet, nonmagnetic
rf	radio frequency
PSD	power spectral density

List of Abbreviations (continued)

PSSW	perpendicular standing spin wave
Py	permalloy ($Ni_{80}Fe_{20}$)
RBW	resolution bandwidth
RIE	reactive ion etching
SEM	scanning electron microscope
SHE	spin Hall effect
SHNO	spin Hall nano-oscillator
SIMS	secondary ion mass spectrometry
ST-FMR	spin-torque ferromagnetic resonance
STO	spin-torque oscillator
STT	spin-transfer torque
SV	spin valve
SW	spin wave
TMR	tunneling magnetoresistance
VBW	video bandwidth
YIG	yttrium iron garnet ($Y_3Fe_5O_{12}$)

Publications

List of manuscripts and papers included in this thesis:

I **P. Dürrenfeld**, F. Gerhard, R. K. Dumas, M. Ranjbar, C. Gould, L. W. Molenkamp, J. Åkerman, "*Tunable damping and exchange stiffness of half-Heusler NiMnSb thin films*", manuscript in preparation (2015)

Contributions: FMR measurements and data analysis. AGM measurements. Contributed to writing the manuscript.

II S. R. Sani, **P. Dürrenfeld**, S. M. Mohseni, S. Chung, J. Åkerman, "*Microwave Signal Generation in Single-Layer Nano-Contact Spin Torque Oscillators*", IEEE Trans. Magn. **49** no. 6, 4331 (2013)

Contributions: Part of device fabrication (EBL). Microwave emission measurements. Data analysis. Contributed to writing the manuscript.

III **P. Dürrenfeld**, S. M. Mohseni, F. Gerhard, M. Ranjbar, F. Qejvanaj, S. R. Sani, S. Chung, C. Gould, L. W. Molenkamp, J. Åkerman, "*Low-Current, Narrow-Linewidth Microwave Signal Generation in Single-Layer-NiMnSb Based Nano-Contact Spin Torque Oscillators*", manuscript in preparation (2015)

Contributions: Device fabrication. AGM and FMR characterization. Microwave emission measurements. Data analysis. Contributed to writing the manuscript.

IV **P. Dürrenfeld**, F. Gerhard, M. Ranjbar, C. Gould, L. W. Molenkamp, J. Åkerman, "*Spin Hall effect-controlled magnetization dynamics in NiMnSb*", J. Appl. Phys. **117**, 17E103 (2015)

Contributions: Device design. Device fabrication. ST-FMR and AMR measurements. Data analysis. Contributed to writing the manuscript.

V M. Ranjbar, **P. Dürrenfeld**, M. Haidar, E. Iacocca, M. Balinskiy, T. Q. Le, M. Fazlali, A. Houshang, A. A. Awad, R. K. Dumas, J. Åkerman, "*CoFeB-Based Spin Hall Nano-Oscillators*", IEEE Magn. Lett. **5**, 3000504 (2014)

Contributions: Device design. Device fabrication. AMR measurements. Contributed to microwave emission measurements, data analysis, and writing the manuscript.

VI **P. Dürrenfeld**, A. A. Awad, A. Houshang, M. Dvornik, E. Iacocca, M. Ranjbar, R. K. Dumas, J. Åkerman, "*Spin Hall nano-oscillators in*

oblique magnetic fields", manuscript in preparation (2015)

Contributions: Device design. Material deposition. Device fabrication. AMR and microwave emission measurements. Data analysis. Contributed to writing the manuscript.

VII A. A. Awad, **P. Dürrenfeld**, A. Houshang, R. K. Dumas, J. Åkerman, "*Mutually synchronized spin Hall nano-oscillators*", manuscript submitted (2015)

Contributions: Material deposition. Device fabrication. AMR measurements. Contributed to microwave emission measurements, data analysis, and writing the manuscript.

List of papers related to, but not included in this thesis:

1 **P. Dürrenfeld**, E. Iacocca, J. Åkerman, P. K. Muduli, "*Parametric excitation in a magnetic tunnel junction-based spin torque oscillator*", Appl. Phys. Lett. **104**, 052410 (2014)

2 **P. Dürrenfeld**, E. Iacocca, J. Åkerman, P. K. Muduli, "*Modulation-mediated unlocking of a parametrically phase-locked spin torque oscillator*", Appl. Phys. Lett. **105**, 252404 (2014)

3 E. Iacocca, **P. Dürrenfeld**, O. G. Heinonen, J. Åkerman, R. K. Dumas, "*Mode-coupling mechanisms in nanocontact spin-torque oscillators*", Phys. Rev. B **91**, 104405 (2015)

4 R. Sharma, **P. Dürrenfeld**, E. Iacocca, O. G. Heinonen, J. Åkerman, P. K. Muduli, "*Mode-hopping mechanism generating colored noise in a magnetic tunnel junction based spin torque oscillator*", Appl. Phys. Lett. **105**, 132404 (2014)

5 T. Chen, **P. Dürrenfeld**, S. Rodriguez, J. Åkerman, A. Rusu, "*A highly tunable microwave oscillator based on MTJ STO technology*", Microw. Opt. Technol. Lett. **56**, 2092–2095 (2014)

6 A. Houshang, M. Fazlali, S. R. Sani, **P. Dürrenfeld**, E. Iacocca, J. Åkerman, R. K. Dumas, "*Effect of Excitation Fatigue on the Synchronization of Multiple Nanocontact Spin-Torque Oscillators*", IEEE Magn. Lett. **5**, 3000404 (2014)

7 R. K. Dumas, S. R. Sani, S. M. Mohseni, E. Iacocca, Y. Pogoryelov, P. K. Muduli, S. Chung, **P. Dürrenfeld**, J. Åkerman, "*Recent Advances in Nanocontact Spin-Torque Oscillators*", IEEE Trans. Magn. **50** no. 6, 4100107 (2014)

Acknowledgments

The research work contained in this thesis is the result of my more than 4 years at the University of Gothenburg. It goes without saying that it is not the work of only one individual, it rather originates from teamwork with my colleagues. They make this place an inspiring environment for research and help me to accomplish my studies.

My foremost acknowledgment goes to my supervisor and group leader Johan Åkerman. His ideas and motivations are the driving force behind the immense growth that the group and the laboratories have undergone during my time here. Under his supervision I learned a lot, especially about the key factors of systematic research, publishing, and networking. He also funded and motivated my participation in a number of summer schools and conferences over the world, which have been beneficial to both education and research.

Furthermore I'd also like to thank the two senior researchers of the group, Randy Dumas and my co-supervisor Pranaba Muduli. They have made indispensable contributions to my development by sharing their valuable laboratory skills as well as driving the evolution of the labs into one of the world's best places of spintronics research. A special thanks also to Ezio Iacocca as a long-standing colleague, for his initial and continued guidance through the Ph. D. education at the University of Gothenburg, and for collaborating on our publications with competent analytical and numerical calculations.

Special thanks go to my Ph. D. examiner Robert Shekhter as well as to the head of the Department of Physics, Mattias Goksör. I'd also like to extend my gratitude towards the administration of the department for navigating through the necessary paperwork: Bea Augustsson, Maria Siirak, and Johanna Gustavsson.

I will not forget to thank for the state-of-the-art cleanroom equipment being available in Chalmers, MC2 department. In connection to that, many thanks go to the cleanroom staff: Bengt Nilsson, Mats Hagberg, Johan Andersson, Piotr Jedrasik, and Ulf Södervall, since the tools would be less useful to me without their great knowledge and support.

Going back to the beginning of my Ph. D. studies and being the only group member working in the MC2 cleanroom, it was of great help to receive remote assistance and feedback from my fabrication colleagues at KTH, Stockholm: Sohrab Sani, Johan Persson, and Majid Mohseni. Also a special thanks to Afshin Houshang for taking over so much of the fabrication work in the recent time.

For machining helpful parts for our measurement laboratory I'd like to thank Jan-Åke Wiman as well as Mats Rostedt for software support and

installation work, thus keeping the labs working at the highest possible level.

I'm also very thankful for having worked with all my colleagues from different parts of the world who are making the research life more enjoyable: Michael Balinsky, Mojtaba Ranjbar, Ahmad Awad, Mykola Dvornik, Mohammad Haidar, Yevgen Pogoryelov, Yuli Yin, Yeyu Fang, Martina Ahlberg, and Masoumeh Fazlali at the University of Gothenburg; Tuan Le, Sunjae Chung, Fatjon Qejvanaj, Anders Eklund, Anh Nguyen, Fredrik Magnusson, and Amir Banuazizi at KTH and Nanosc AB.

Many thanks to Experimentelle Physik 3 at Universität Würzburg for the fruitful collaboration and for growing high quality films, namely to Felicitas Gerhard, Charles Gould, and Laurens W. Molenkamp.

Einen besonderen Dank an meine Eltern, meine Großeltern, meinen Bruder, weitere Familie und Freunde für die Unterstützung und das im Kontakt bleiben über die Distanz.

Introduction

The high-speed communication of data is crucial for the future development of the world's prosperity, and has already experienced extraordinary growth over the last few decades. By the time data finally reaches one's smartphone or computer, it has passed through a long chain of processing, storage, and communication in logic circuits. These logic circuits are today almost exclusively based on complementary metal-oxide-semiconductor (CMOS) technology, relying on the presence or flow of electron *charges* in nanodevices. However, with increasing operation frequencies and further miniaturization of CMOS devices, this technology is approaching its limits due to the ever increasing power that is needed to pass more electron charge currents. Alongside the charge of electrons, it is therefore necessary to make use of the intrinsic magnetization of the electron, which arises from the quantum-dynamic property of *spin*, as an additional parameter to manipulate. This approach leads to the field of spintronics [1, 2].

These spintronic technologies, still in their infancy in terms of implementation in market applications, have opened up a wide array of research concepts. One of these is the field of magnonics (the magnon is the quantization of a spin wave), in which logic functions are implemented by the generation, manipulation, and analysis of spin waves [3, 4]. It has been shown that spin-transfer torque (STT) driven oscillations in extended magnetic multilayers can act as nanoscopic sources of high-frequency spin-wave modes [5, 6], such as propagating spin waves [7, 8, 9, 10], spin-wave bullets [11, 12, 13, 14], and magnetic droplets [15, 16, 17]. All of these findings relied on the presence of a material system with at least 2 magnetic layers: one acting as a spin polarizer and one as the free layer in which the actual spin-wave dynamics are excited. However, it is clear that the presence of multiple magnetic films introduces complexity into the device fabrication, as well as in the dynamics themselves, as both layers mutually influence each other. Removing these complexities by shifting towards STT-induced spin-wave generation in devices that consist of only one FM layer—while also improving the device characteristics in terms of spin-wave power, frequency, and linewidth—are therefore important goals in driving forward the development of magnonic logic circuits [18, 19, 20].

The dynamics of spin valve (SV-) and magnetic tunnel junction (MTJ-) spin-torque oscillators (STOs) have been widely studied in terms of applications, such as spin-wave propagation [21], mutual synchronization [22, 23, 24], modulation [25, 26, 27, 28], injection locking [29, 30, 31], and parametric excitation [32, 33, 34]. More recently, the implementation of the spin Hall effect (SHE) [35] as the driving mechanism in STOs, has become increasingly

popular [36, 37, 38]. This development opens up the possibility of new device layouts with in-plane currents and easier access to the spin-wave dynamics by optical methods such as microfocused Brillouin light scattering (μ-BLS). Additionally, these so-called spin Hall nano-oscillators (SHNOs) have the intrinsic advantage of incorporating only one ferromagnetic (FM) layer, which can even be an insulator, as no current flow through the FM is required.

This thesis aims to drive the applicability of STOs and SHNOs as spintronic high-frequency generators forward, and the work is therefore focused on (a) materials and devices with low linewidths and high output powers, and on (b) simplifying device fabrication by using single ferromagnetic layer structures. Both paths can work hand-in-hand, as it has been shown, for example, that the low-damping half-metallic material NiMnSb can be straightforwardly implemented in single-layer NC-STOs and SHNOs.

This thesis is organized as follows:

Chapter 1 contains an introduction to the underlying physical effects, which are needed to understand the experimental results in this thesis. Furthermore, the applied measurement techniques will be introduced, and there is a dedicated section describing the process of fabrication of SHNOs. Deposition and lithography techniques will be introduced in more detail, where applicable.

Chapter 2 focuses on single-layer NC-STOs; auto-oscillation dynamics have been obtained in this layout for permalloy (Py) films, as well as for films from the low-damping half-Heusler alloy NiMnSb. The Py-based devices show reliable low-frequency (0.25 GHz to 3 GHz) oscillations that most likely stem from vortex–antivortex excitations (gyration, generation, and annihilation), as they have a high number of measurable harmonics and are straightforwardly observed in zero applied magnetic field. On the other hand, among the striking features of NC-STOs based on NiMnSb are their relatively high frequencies (up to 6 GHz) combined with their record low oscillation linewidths of $\approx$500 kHz. However, these auto-oscillations need a nearly perpendicular magnetic field between 1000 Oe and 7000 Oe. A bigger drawback is that the samples display low device-to-device repeatability, showing references to spin-torque excitations in mechanical point contacts.

Chapter 3 then covers SHNOs and fundamental studies on their underlying physics that lead into auto-oscillations. Sharp-tip gold electrodes were used as localized current injectors into a Pt layer on top of various materials, such as Py, $Cu_{40}Fe_{40}B_{20}$, and NiMnSb. It is shown that, for in-plane applied fields, the auto-oscillation modes have relatively broad linewidths with frequencies close to ferromagnetic resonance (FMR). The magnitudes of measured output signals are directly related to the anisotropic magnetoresistance (AMR) in the FM layer, which among these materials is undoubtedly the largest for Py. The SHNOs based on Py are then further investigated in tilted magnetic fields showing low-linewidth auto-oscillations, which are clearly identified as nonlinear spin-wave bullets.

Chapter 4 extends the research on spin-wave bullets in SHNOs by synchronizing them in order to increase the output power and reduce the linewidth even more. In SHNOs based on double-needle Au electrodes, the current flow

generates two parallel bullets that mutually synchronize via the extended free layer. Another synchronization scheme is achieved in nanoconstriction SHNOs, where the serial connection of numerous constrictions yields the mutual synchronization of up to nine devices.

1

Background and Techniques

1.1 Basic Physical Effects

1.1.1 Spin Hall Effect

Edwin H. Hall discovered in 1879 that a current subjected to a transverse magnetic field yields a measurable voltage on the sides of the conductor [39]. This effect, known as the Hall effect, can be understood as the Lorentz force acting on the moving electrons. Shortly thereafter, Hall discovered a similar effect in the ferromagnetic materials nickel (Ni) and cobalt (Co), in which the transverse voltage depends not only on the magnetic field, but also on the magnetization of the material [40]. This effect is known today as the anomalous Hall effect (AHE) and provides direct evidence of spin-dependent forces with opposite sign to the electrons, which due to the net spin polarization in the ferromagnetic material shows itself as a charge imbalance on the sides of the conductor. However, transverse, spin-dependent forces are also present in nonmagnetic materials, leading to the separation of electrons of opposite spin towards the edges of the material slab without a charge imbalance. This behavior is thus called the spin Hall effect (SHE) [35] and was first described by D'yakonov and Perel' in 1971 [41]. The first direct experimental observation of the SHE occurred in 2004 by magneto-optical detection of the spin accumulation in a semiconductor [42, 43], and in 2007 the first electric detection in an Al stripe was successfully demonstrated [44].

The underlying mechanisms that lead to the SHE and AHE are of purely quantum-mechanical origin, and stem from spin-orbit interactions. They remain an active area of research. Three main sources can be identified [45], of which one is the intrinsic spin Hall effect resulting from the effects of spin-orbit interaction on the band structure of the metal, thus leading to forces on the electrons between scattering events [46]. Unlike the intrinsic spin Hall effect, spin-skew scattering [47] and side-jump scattering [48] are both considered extrinsic effects, as they rely on the presence of scattering events and are therefore highly dependent on material impurities [49]. While the spin-skew

scattering can be described as an effective field gradient—and therefore as a spin-dependent acceleration—on the scattering side, side-jump scattering is understood as a small dislocation of the electrons of opposite spin summing up over subsequent scattering events.

The spin Hall effect can be quantified by the spin Hall angle [45]

$$\Theta_{SH} = \frac{\sigma^s_{xy}}{\sigma^c_{xx}} \frac{e}{\hbar}, \tag{1.1}$$

where σ^s_{xy} is the so-called transverse spin Hall conductivity and σ^c_{xx} is the longitudinal charge conductivity of the material. Spin Hall angles are usually given in the unit of % and in a material with a positive Θ_{SH}, the magnetic moments of the spin accumulation along the edges follow the right-hand rule with the charge current direction. The oppositely directed left-hand rule applies to materials with a negative sign on the spin Hall angle.

Absolute values as high as $|\Theta_{SH}|$=33 % have been reported for a thin-film device with β-W [50] and the search for even larger spin Hall angles in, for example, alloyed materials is ongoing. However, platinum (Pt) is certainly the most commonly used material for implementing the SHE, on account of its relatively high spin Hall angle in combination with its high conductivity and the ease of material synthesis. Recent research has found a model based on band-structure calculations—that is, on the intrinsic spin Hall effect—for the 4d and 5d transition metals, which consistently explains the measured spin Hall angles [51, 52, 53]. Transition metals with less than half-filled d-orbitals, such as Ta and W, can be explained as experiencing a negative spin Hall angle, while materials with greater than half-filled d-orbitals, such as Pt and Pd, have positive spin Hall angles.

1.1.2 Anisotropic Magnetoresistance

The dependence of the electric resistance of ferromagnetic materials on the orientation between current flow and magnetization was discovered as early as 1856 by William Thomson (Lord Kelvin) [54]. The angular dependence of the resistance is described by:

$$\rho = \rho_\perp + (\rho_\parallel - \rho_\perp) \cos^2 \theta, \tag{1.2}$$

where $\rho_\parallel$ ($\rho_\perp$) stands for the resistivity at parallel (perpendicular) orientation between magnetization and current direction, and θ describes an arbitrary angle between both. The AMR ratio $(\rho_\parallel - \rho_\perp)/\rho_\perp$ of the majority of materials, such as permalloy, is typically positive and has its maximum on the order of a few percent [55]. However, examples of materials with a negative AMR ratios include half-metallic ferromagnets, such as the Heusler materials Co_2(Fe,Mn)Si [56] and NiMnSb, which is used in this thesis. Due to the presence of only one spin direction on the Fermi level in half-metals, the otherwise dominant s-d electron scattering processes with spin-flip are impossible; these are otherwise responsible for the positive AMR sign in most magnetic materials [57].

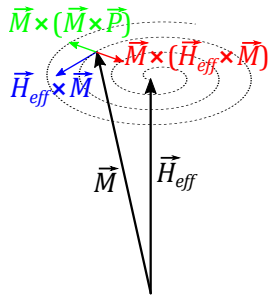

Figure 1.1: Illustration of the terms in the Landau–Lifshitz–Gilbert–Slonczewski equation (eq. 1.3). The first (blue) term leads to a circular precession around $\vec{H}_{eff}$, while the second (red) contribution describes the Gilbert damping, which leads to a damped spiral movement, as shown by the dashed black line. The third (green) term is the spin-transfer torque, which can compensate the damping for sufficiently large spin-polarized currents.

1.1.3 Spin-Transfer Torque

Magnetization dynamics in spintronic devices are best analytically described by the Landau–Lifshitz–Gilbert equation [58] with an additional spin-torque term. This was first described by Slonczewski [6] and Berger[5] in 1996:

$$\frac{\partial\vec{M}}{\partial t} = -\gamma\left(\vec{M}\times\vec{H}_{eff}\right) - \frac{\gamma\alpha}{M_0}\left[\vec{M}\times\left(\vec{M}\times\vec{H}_{eff}\right)\right] + \tau\left[\vec{M}\times\left(\vec{M}\times\vec{P}\right)\right], \tag{1.3}$$

where $\vec{P}$ is a vector pointing along the spin polarization of the incoming current. The first term in eq. 1.3 describes an undamped precessional motion around the effective field vector $\vec{H}_{eff}$, while the second term results in a damping vector directed towards $\vec{H}_{eff}$; this would lead to an eventual parallel alignment with $\vec{M}$. The third term describes a current-induced torque, which is oriented antiparallel to the Gilbert damping, resulting from the nonparallel alignment of the current polarization $\vec{P}$ with $\vec{M}$. Given the opposite directions of the two latter terms, the spin-transfer torque can equalize the damping for large enough currents, and thus result in an undamped (that is, steady) oscillation in the ferromagnet. The directions of the three terms in eq. 1.3 are illustrated in Fig. 1.1

Initially, the only source of spin polarization was the current flowing through two spatially separated layers of ferromagnets, as shown in Fig. 1.2(a). In these trilayer ("spin valve") structures, the electrons are polarized while moving through a *fixed* ferromagnetic layer, followed by a nonmagnetic spacer layer that is thinner than the spin-flip length of the electrons. Finally, the thus-polarized current enters a *free* magnetic layer, where the generally nonparallel alignment between polarizer and free layer results in the above described spin-transfer torque. The magnetization in the fixed layer is in this way stabilized, either via a large saturation magnetization M_0 or a large volume; alternatively,

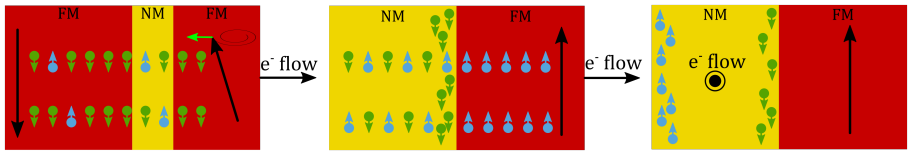

(a) spin valve structure (b) single ferromagnetic layer (c) spin Hall effect

Figure 1.2: The common technological means for achieving STT-driven devices are as follows. **(a)** In a spin-valve structure, the current is spin-polarized as a result of it flowing through a fixed layer, which applies a spin torque (the green arrow) to the exchange-decoupled free layer. **(b)** An unpolarized current from a nonmagnetic material becomes polarized as it flows into a ferromagnet, leaving behind the accumulated spins of the opposite sign at the interface. **(c)** A current flowing through a nonmagnetic material leads to spin accumulation at its interfaces, due to the spin Hall effect. In cases of **(b)** and **(c)**, the accumulated spins can then diffuse into the ferromagnet, which results in a torque. Note that, in the case of **(c)**, no current flow through the ferromagnet is required.

it is exchange-biased [59] to an adjacent antiferromagnet.

Recently, alternative approaches to the generation of spin-polarized currents, and thus of spin-transfer torque, have been successfully implemented by relying on spin accumulation in an adjacent nonmagnetic metal, rather than on the spin filtering described above. This accumulation can be achieved as an intrinsic consequence of the spin filtering in a ferromagnet when current passes through the NM–FM interface [60, 61] (see Fig. 1.2(b)), and has been used for spin-torque-induced oscillations in *single* ferromagnetic layers [62, 63, 64, 65]. The spin Hall effect (see section 1.1.1) in nonmagnetic metals is also presently being used as an effective source of spin accumulation [66, 67, 68, 69], in which no current flow into a ferromagnetic material is required, as illustrated in Fig. 1.2(c). This effect thus also makes it possible to expand the available materials for spintronic devices to include ferromagnetic insulators [70].

1.2 Measurement Techniques

1.2.1 Ferromagnetic Resonance

The term *ferromagnetic resonance* (FMR) describes the collective movement of the magnetization in a ferromagnetic material in an external magnetic field. An analytical description can be thus obtained by treating the individual spins as one macroscopic spin. The precession of a magnetization vector around a magnetic field $\vec{B}$ follows from the differential equation [71]

$$\frac{d\vec{M}}{dt} = -\gamma(\vec{M} \times \vec{B}), \tag{1.4}$$

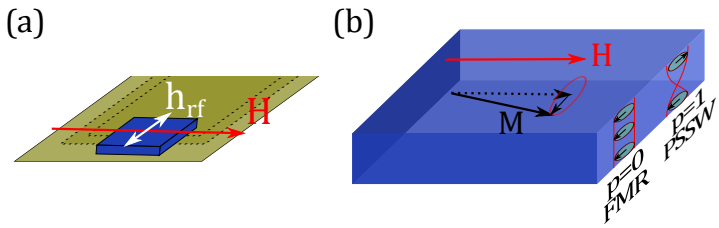

Figure 1.3: (a) Illustration of an FMR measurement setup utilizing a coplanar wave guide (CPW) for rf excitation. (b) For sufficiently thick films, besides the uniform FMR mode with $\vec{k}$=0, perpendicular standing spin waves (PSSW) are also excited, which have a thickness-dependent oscillation amplitude and phase.

which is simply the first term of eq. 1.3, and leads to a precessional motion with Larmor frequency $\gamma/2\pi B$. However, in ferromagnetic materials, and more specifically in thin films, the demagnetization fields need to be taken into account in addition to the external applied field. For the general case of a thin film magnetized in an arbitrary out-of-plane angle, the field dependence of the resonance frequency f_0 yields [12]

$$f_0 = \frac{\gamma\mu_0}{2\pi}\sqrt{H_{int}\left(H_{int} + M_0\cos^2\theta_{int}\right)}, \tag{1.5}$$

where H_{int} and θ_{int} are the internal field and the out-of-plane tilting, respectively, and can be calculated from the external applied field H_{ext} and its angle θ_{ext} by solving for the magnetostatic boundary conditions:

$$\begin{aligned} H_{ext}\cos\theta_{ext} &= H_{int}\cos\theta_{int} \\ H_{ext}\sin\theta_{ext} &= (H_{int} + M_0)\sin\theta_{int}. \end{aligned} \tag{1.6}$$

For $\theta_{int} = 0$ eq. 1.5 transforms into the well-known Kittel equation for an in-plane magnetized thin film [72, 73, 74]. Depending on the specific case, anisotropy and exchange fields also need to be introduced for an accurate description [75] as can be seen (for example) in Ref. [76].

It is notable that the FMR condition describes a spin wave with an infinitely large wavelength—that is, a minimal wave vector $\vec{k} = 0$. The FMR frequency thus represents an important distinction between propagating and localized oscillation modes in spintronic devices. While localized spin-wave modes with a frequency below FMR have no available wave vector in the distant region and therefore fade out [11], propagating modes have a frequency higher than FMR and can therefore propagate for several µm within the ferromagnet with a finite $\vec{k}$ vector [10].

Experimentally, FMR frequencies are determined by applying an in-plane microwave field h_{rf} oriented perpendicularly to the dc applied field. In the resonance condition $f_{rf} = f_0$, energy from the rf source is absorbed into the metallic thin film, as in a classical driven damped oscillator. The signal observed in the FMR setup—which utilizes a coplanar waveguide (CPW) for excitation and a lock-in technique for signal detection [Fig. 1.3(a)]—corresponds

to the derivative of the absorbed rf power around the resonance field. It can be described by the derivative of an asymmetric Lorentzian function [77, 78]:

$$\frac{dP}{dH}(H) = \frac{-8K_1\Delta H(H-H_0) + 2K_2\left(\Delta H^2 - 4(H-H_0)^2\right)}{\left[\Delta H^2 + 4\left(H-H_0\right)^2\right]^2}, \tag{1.7}$$

where K_1 and K_2 are fitting parameters for the symmetric and antisymmetric Lorentzian parts, respectively. The CPW is designed to only excite spin-wave modes with an in-plane wave vector $\vec{k} \to 0$. Thus, besides the uniform FMR mode, exchange-dominated perpendicular standing spin waves (PSSW) can also be excited [79]. Their resonance field is shifted by an exchange field $H_{ex} = \frac{2A}{M_0}\left(\frac{p\pi}{d}\right)^2$ w.r.t. the FMR mode, where d is the thickness of the film, A is the exchange stiffness and p is the integer order of the PSSW mode. PSSWs are characterized by a thickness-dependent spin-wave amplitude and phase [80], which is schematically shown in Fig. 1.3(b) for $p = 1$. It is therefore possible to extract the exchange stiffness of sufficiently thick films by in-plane FMR measurements, where the knowledge of H_{ex} is readily obtained for high enough frequencies [81]. This technique has been used in manuscript **I** for a study on the exchange stiffness in NiMnSb half-Heusler films of varying composition.

Finally, the frequency dependence of the peak linewidth ΔH in a swept magnetic field also yields information directly about the intrinsic Gilbert damping constant α through the linear dependence [82]:

$$\Delta H = \Delta H_0 + \frac{4\pi}{\gamma}\alpha f_0. \tag{1.8}$$

1.2.2 Spin-Torque Ferromagnetic Resonance

In current-driven nanoscale devices, it is also possible to excite ferromagnetic resonance oscillations through the application of a subthreshold microwave current [83, 84, 85, 86], rather than by using an external microwave field, as described for extended films in section 1.2.1. The driving force behind the excitation in this case is then the periodic spin-transfer torque (term three of eq. 1.3), which effectively reduces the damping in the case of $f = f_0$. The collective precession of the spins in the free layer leads in turn to a time-varying resistance, due to the AMR effect in the case of SHNOs (see section 1.1.2). This time-varying resistance, multiplied by the applied microwave current of the same frequency, yields (via trigonometric relations amongst other terms) a *dc* mixing voltage that can be readily measured. The magnitude of the observed voltage is typically small, on the order of µV, and it is therefore common to include a lock-in type measurement for an enhanced signal-to-noise ratio by modulating the amplitude of the microwave current—for example, with a pulsed signal, as illustrated in Fig. 1.4. In the case of SHE-driven excitations in NM/FM bilayers, the mixing voltage around the resonance field follows, according to Refs. [87, 68], an asymmetric Lorentzian function:

$$V_{mix} \propto S\frac{\Delta H^2}{\Delta H^2 + 4(H-H_0)^2} + A\frac{2\Delta H(H-H_0)}{\Delta H^2 + 4(H-H_0)^2}, \tag{1.9}$$

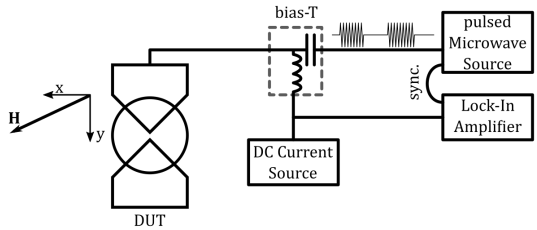

Figure 1.4: Schematic drawing of the ST-FMR measurement setup. The microwave source provides a pulsed output with a modulation frequency of ≈100 Hz, which is synchronized to the lock-in amplifier for detection of the resulting dc mixing voltage, while the external field is swept.

from which, by the relation between the amplitudes of the symmetric (S) and antisymmetric (A) parts of the Lorentzian, the spin Hall angle Θ_{SH} can be estimated:

$$\Theta_{SH} = \frac{J_{S,rf}}{J_{C,rf}} = \frac{S}{A}\frac{e\mu_0 M_0 d_{NM} d_{FM}}{\hbar}\sqrt{1+\frac{M_{eff}}{H_0}}. \tag{1.10}$$

Here d_{NM} and d_{FM} represent the thickness of the NM and FM layer, respectively.

1.2.3 Electrical High-Frequency Measurement

The NC-STO and SHNO devices described in this thesis are characterized via their electrical microwave signal generation, following from the spin-torque-driven precession of the magnetization. This precession leads to a time-varying angle between the bias current and the magnetization, and thus to a rapid (in the GHz range) oscillation of the device resistance through the AMR in the FM layer. This can, in turn, be detected as an ac voltage signal, which is experimentally decoupled from the applied bias current by the use of a broadband (dc to 40 GHz) bias tee, as shown in the measurement circuit in Fig. 1.5. As the generated signals have very low power spectral density (PSD), the use of a low-noise amplifier (LNA) with a gain of ≥32 dB and a noise figure on the order of ≤3 dB is needed to raise the power of the signals above the noise floor of the spectrum analyzer and to thus make them detectable. The spectrum analyzer used throughout this thesis is a Rohde & Schwarz FSV-40, commonly operated in frequency sweep mode with a resolution bandwidth (RBW) of 1 MHz and a video bandwidth (VBW) of 10 kHz. The combination of a Keithley 6221 current source with a Keithley 2182A nanovoltmeter has functioned as the main dc current source. However, Keithley 2400 and 2450 stand-alone source meters have also been successfully implemented into the measurement setup without noticeable differences.

The spectra obtained in the frequency domain are post-processed using the MATLAB programming framework, where they are first corrected for amplifier gain and for losses from the apparent impedance mismatch that results

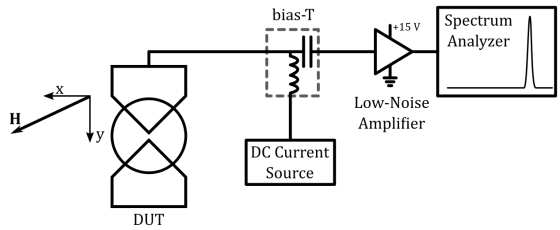

Figure 1.5: Schematic drawing of the measurement setup needed to detect microwave auto-oscillation in STOs and SHNOs. The applied dc bias results in auto-oscillation signals captured at the rf port of the bias tee and amplified by an LNA to raise their levels above the noise floor of the spectrum analyzer. The external field can be applied using electromagnets or permanent magnets in various in-plane and out-of-plane directions.

from the fixed $50\,\Omega$ impedance in the rf measurement circuit in connection with the varying resistance of the devices. The auto-oscillations that occur in the spectra are then fitted with a symmetric Lorentzian function, yielding accurate measures of the oscillation frequencies, the full-width-at-half-maximum (FWHM) linewidths, and the integrated output power.

1.2.4 Microfocused Brillouin Light Scattering

Besides the FMR measurements, Brillouin light scattering (BLS) is a technique frequently used in the study of spin waves. The main advantage of the BLS technique over FMR measurements is the possibility it gives of directly observing spin waves in much smaller sample dimensions, limited only by the laser spot size. In BLS measurements, the interactions between photons and magnons—the quanta of light and spin waves, respectively—are the underlying mechanism. An incident photon can annihilate or generate a magnon in an inelastic scattering process in the FM film, thereby gaining or losing, respectively, the energy of the magnon. This gain or loss of energy appears as a shift in frequency and wavelength in the scattered light, which can in turn be analyzed with an interferometer. This interferometer is the central part of the BLS measurement setup, as it needs to have a very high frequency resolution to distinguish between the manifold spin-wave modes.

The SHNOs in this thesis have been measured using a room-temperature microfocused BLS (μ-BLS) setup, where the incident laser light (532 nm single frequency light) coming from a diode-pumped solid state laser is focused by a dark-field objective (Zeiss, with numerical aperture NA = 0.75). This yields a probing spot size on the order of the diffraction limit—that is, only a few hundreds of nm. Spatially resolved maps of the magnetization dynamics are then generated by scanning the sample underneath the probing spot with a three-dimensional scanning stage. The scattered light is analyzed using a six-pass Tandem Fabry-Perot TFP-1 interferometer (JRS Scientific Instruments) and the frequency-resolved intensities are acquired on the measurement computer

using a single photon counter. The obtained BLS intensity is proportional to the square of the amplitude of the magnetization dynamics at the corresponding frequency. Moreover, the μ-BLS setup is equipped with a spectrum analyzer connected to the sample via a bias tee to observe microwave electrical signals simultaneously with the optical signals.

1.3 Fabrication of Spin Hall Nano-Oscillators (SHNO)

Although the fabrication of NC-STOs has been previously developed in our work group and is described in Ref. [88], a detailed process for the fabrication of SHNOs needed to be developed. The first published working SHNOs [36] were fabricated on sapphire (Al_2O_3) substrates, as their low electrical output required optimization in terms of microwave losses and thermal conductivity; for both of these factors, sapphire is superior to Si and SiO_2 substrates. However, the optical transparency and very low conductivity of sapphire led to additional precautions being necessary for successful e-beam lithography. Besides the change in substrate, the production of the devices also evolved from a fabrication process on full-sized 100 mm wafers with a large number of chip repetitions to a single-chip process allowing arbitrary substrate sizes down to $\approx$10 mm. This (on the first sight backwards) step was driven by the absence of a lithography stepper in the cleanroom, although in the end, it opened up the possibility of processing thin films received as part of collaborations, where film depositions on large wafers are uncommon. The following sections describe the process used to fabricate the SHNOs used in this work. The choice of different material stacks and substrates leads to a challenge: during the lithographic process, several parameters need to be adjusted accordingly, although the general fabrication scheme (*e.g.*, the resists and etching technologies used) remains the same. The fabrication techniques used here and their application to the process of fabricating both nanoconstriction SHNOs [89] and gold needle SHNOs [36] are briefly described in the following sections.

1.3.1 Film Deposition

Owing to the wide variety of material systems that our SHNOs have been fabricated on—namely $Ni_{80}Fe_{20}$/Pt, $Co_{40}Fe_{40}B_{20}$/Pt, YIG/Pt, and NiMnSb/Pt—the film deposition methods and underlying substrates were also heterogeneous. While in the first two cases, both layers (FM and platinum) were deposited in our AJA sputtering system on sapphire substrate pieces of 20 mm$\times$20 mm, the YIG films were grown externally on GGG substrate and only sputter-deposited with Pt after a thorough cleaning by us. In particular, the Heusler film material was fully grown *in situ* by molecular beam epitaxy and sputtering from the University of Würzburg. When the full film stack is deposited on sapphire substrate pieces, no additional substrate preparation steps (*e.g.,* etching or annealing) are needed, except a general cleaning by water rinsing in order to remove particles.

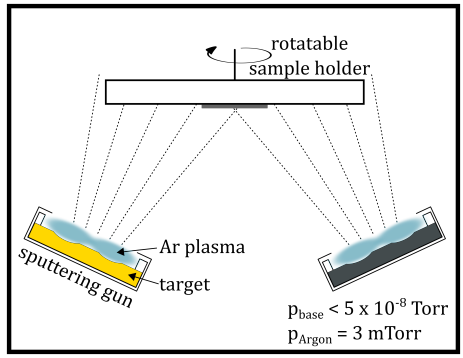

Figure 1.6: Illustration of the sputtering chamber used for fabrication. At the bottom of the vacuum chamber are 7 sputtering guns circularly arranged to deposit confocally onto the sample holder. Each gun is equipped with a shutter, which is not illustrated here. Up to three guns can be activated simultaneously, allowing for codeposition of alloyed materials.

Sputtering was performed in an AJA Phase II system, consisting of a high vacuum (HV) chamber, equipped with 7 confocal sputtering guns arranged circularly in the bottom of the vacuum chamber. The samples are mounted facing down onto the substrate holder and transferred via a load lock into the vacuum. Up to three of the 7 guns can be activated simultaneously, making thin-film deposition of alloys possible.

1.3.2 Alignment Mark Fabrication

A key point in obtaining a consistent process between the different substrate materials is the choice of the size and (more importantly) the material of the alignment marks. The limiting factor here was the use of the e-beam lithography system and its semiautomated procedure of substrate aligning for a large part of the processing. The alignment mark detection works through a change in the detected secondary electrons when the electron beam is scanned over a leg of the alignment cross. Making use of just the material stack as the alignment mark material would give rise to uncertainty in each processing, as the contrast of the very thin films (sometimes thinner than 10 nm) might not be sufficient for automated detection. The contrast is directly related to the physical height of the mark, as well as to a material contrast in terms of the atomic number Z, between the underlying substrate and the alignment mark. To have a working set for all our processed substrates, it was therefore decided to fabricate relatively thick, high-Z material alignment marks in a lift-off process prior to all other lithographic steps.

A 100 nm layer of the MicroChem LOR1A lift-off spacer and a 1.3 µm layer of S1813 photoresist are for this reason first coated and soft-baked onto the material pieces. After exposure in the mask aligner, the lift-off layer develops with a faster speed than the photoresist, leaving behind an undercut in the

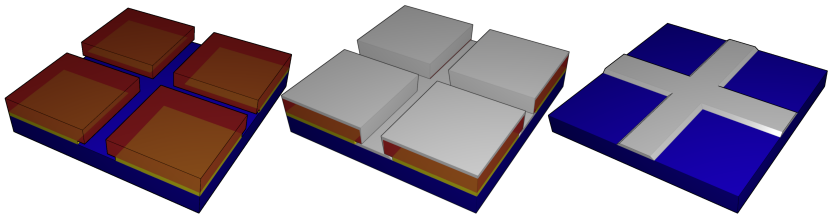

Figure 1.7: The three steps of the lift-off process using the example of alignment mark fabrication. (a) Positive photoresist with an lift-off layer underneath leads to an undercut. (b) Film deposition covers the whole sample as well as the photoresist, but the lift-off layer prevents a closed film surface. (c) Dissolving the resist layers leaves behind the desired structure.

bilayer (see Fig. 1.7(a)). The pieces are then sputter-deposited in the AJA system with an ≈80 nm thick layer of tantalum (Ta), Fig. 1.7(b) and the lift-off is performed in a warm bath of photoresist remover with intermittent ultrasonic agitation. This technique leaves behind the desired alignment marks on top of the substrate and the previously sputtered extended material stack, as depicted in Fig. 1.7(c). The time needed to achieve a clean lift-off is strongly dependent on the amount and type of agitation, and can vary from several minutes to ≈1 hour. Tantalum was chosen due to its high atomic number of Z=73 and its good adhesion to most substrate materials, coupled with its drastically lower material price than other options, such as Au or Pt.

1.3.3 SHNO Mesa Fabrication

As a second step, it is necessary to pattern the devices' active area—*i.e.*, a circularly shaped mesa into which the spin waves can expand, analogous to the extended free layer in an NC-STO. Alternatively—using the same fabrication method—we can form nanoconstrictions in the FM–NM bilayer material. In these structures, the in-plane current is focused to a nm-sized region by the absence of conducting material, similarly to nanopillar (MTJ-)STO devices based on a spin-valve structure.

As the metal bilayer was initially deposited as an extended film, this patterning always occurs as an etching step. The need for controlled etching of lateral dimensions on the order of tens of nm, especially in the case of nanoconstriction, as well as the inclusion of noble metals in our material stack, excludes the possibility of a wet etching technique and leaves ion beam etching (IBE) as the tool of choice for this step. IBE, as one of several dry etching tools, is useful when used alongside reactive ion etching (RIE), as an rf plasma is generated in a separate source, thus reducing the heat load on the sample during etching. This makes it possible to directly use (e-beam) resist as masking material during etching, as long as it is thicker than the material being etched, as there is no material selectivity due to the pure bombardment with noble gas (Ar) atoms. The beam of Ar atoms is generated by extracting positively charged

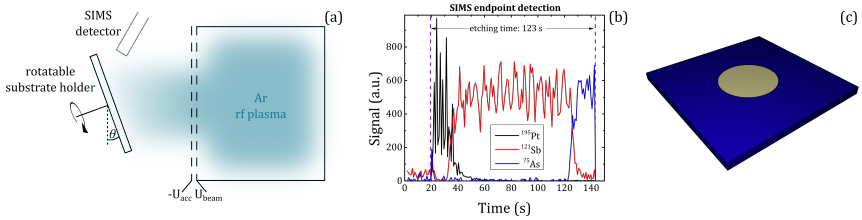

Figure 1.8: Fabrication of the EBL-defined SHNO mesas by ion milling. (a) Schematic drawing of the IBE system. (b) Exemplary SIMS detection signal vs. etching time for a NiMnSb (41 nm)/Pt (6) material stack. (c) Illustration of the 4 µm disk after etching and resist removal.

Ar^+ ions from the remote plasma by two aligned grids placed in front of it, and immediately neutralizing those with a beam of electrons in front of the source, thus also eliminating the possibility of charge-induced damage to the sample surface. The sample holder in the IBE vacuum chamber can be tilted between 0° (perpendicular to the beam) and 90° (lateral beam incidence), in order to adjust for etch defects, such as trenching and sidewall deposition [90]. Since, in most cases, we are etching only very thin films ($\leq$15 nm), such defects do not play a significant role and are easily avoided by tilting the sample between θ=10° and 30° with simultaneous rotation (see Fig. 1.8).

The desired patterns are written by electron-beam lithography into the negative resist ma-N 2401 [91, 92], which yields an etching mask $\approx$110 nm thick—sufficient to allow ion milling of all SHNO material stacks that are dealt with in this thesis. The IBE system is equipped with secondary ion mass spectrometry (SIMS) endpoint detection, which is helpful in detecting the speed of the etching *in situ*, and therefore eliminates the need to waste material and time determining the etch rate for each material stack used. A sample SIMS detection curve for the devices from Ref. [93] (manuscript **IV**) is shown in Fig. 1.8(c), where the etching is stopped $\approx$15 s after the substrate material (In,Ga)As is reached.

1.3.4 Gold Needle Fabrication

To focus the current in the center of the SHNOs with a circular mesa, it is necessary to deposit sharp-tip electrodes with a much larger conductance than the material bilayer. This is achieved by the choice of material, here Au, and its great thickness, 150 nm. This lithography step is not needed for nanoconstriction-based SHNOs, as there the current is naturally focused by their shape.

The patterning is done by an EBL lift-off process, where two triangular-based shapes with a tip-to-tip spacing of 50 nm to 300 nm are written on each device. The resist used here is a single layer of the SX ARP 6200/2 positive e-beam resist, which has a thickness of $\approx$220 nm. This was shown to be sufficient for the lift-off. No additional undercut layer (as in section 1.3.2) is used, since this naturally leads to rounding at pattern corners and thus, in

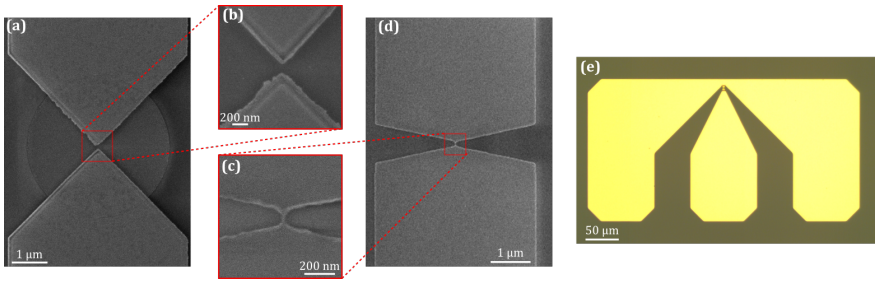

Figure 1.9: Micrographs of fabricated SHNOs. (a) and (b): SEM pictures of an SHNO with a circular mesa and sharp electrode needles after the Au lift-off process. (c) and (d): SEM of nanoconstriction SHNO following ion milling, showing a constriction width of less than 50 nm. (e) Optical micrograph of a full device, including the top waveguide for electrical probing.

our case, a degradation of the sharp electrode tips. Positive resists in EBL also have a small inherent undercut [94], making the lift-off of these nm structures possible. A thin film of Cu on top of the resist is required for reliable EBL on transparent or highly resistive substrates, such as sapphire. This layer could then easily be removed before resist development in a chromium etchant solution.

The electrode material consists of 2 nm Cr as an adhesion-promoting layer, followed by 150 nm Au. Both are sputter-deposited in the same chamber as already described in section 1.3.1. The lift-off is then done in warm resist remover with minimal agitation as a measure to prevent damage to the nanostructures. The process described reliably yields Au electrodes with tip radii of $\leq$30 nm, which are determined by scanning electron microscopy, as in Fig. 1.9(b).

1.3.5 Top Contact Fabrication

In order to easily contact the SHNOs with microwave probes, top contact waveguides with 100 µm wide lines are fabricated around the core devices. The layout of these can be seen in Fig. 1.9(e), where the ratio of 2:1 between the central signal strip width and the adjacent gap to the outer ground lines leads to an rf impedance of $\approx$50 Ω [95], and therefore reasonably good matching to the impedance of the measurement circuit. The top contacts are lithographically fabricated using a lift-off process (Fig. 1.7) employing a $\approx$500 nm thick undercut resist film, which aids the clean lift-off of the $\geq$1 µm thick Cu waveguides.

2

Single-Layer Nanocontact Spin-Torque Oscillators

NC-STOs commonly work on the basis of STT-induced auto-oscillations that are read out either via GMR [96, 97] or TMR [98]. The fabrication of these devices thus requires the deposition of at least two FM metals separated by a metallic or insulating nonmagnetic spacer. This introduces difficulties in the material deposition and increases the thickness of the devices, which can be significant in applications such as hard disks, where the thickness of the reading sensor can limit the bit size and therefore the storage density. Previous studies of mechanical point contacts on magnetic films [62, 99], as well as of single-layer nanopillar devices [100, 63], have shown the presence of STT and its accompanying instabilities. As has been theoretically shown, spin accumulation is achieved by current flowing through the interface between an NM and an FM layer [60, 61], which then also applies spin torque to the FM layer [101]. Thin FM layers with symmetric interfaces are expected to experience no net torque due to the opposite signs on both sides of the layer. However, in the NC-STO geometry, no such symmetries are present, as the current spreads out underneath the NC, yielding different current densities on both sides of the FM layer.

This chapter will describe NC-STOs with one FM layer where, for the first time, STT-driven auto-oscillations could be electrically detected. This layout is shown to work successfully for two material systems: permalloy and the

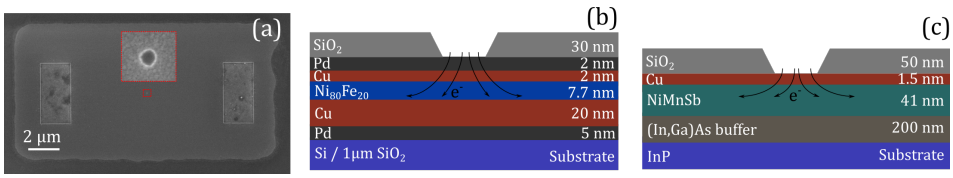

Figure 2.1: (a) SEM micrograph of an NC-STO mesa with the NC (inset) and ground contacts being etched into SiO_2. Schematics of the single-layer NC-STO stacks used: (b) with Py free layer and (c) with NiMnSb free layer.

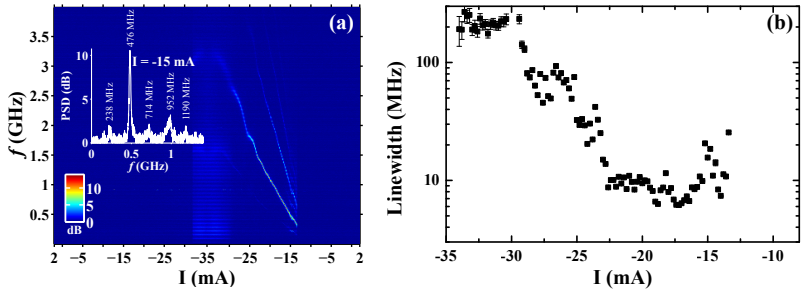

Figure 2.2: Microwave signal of a Py single-layer NC-STO with zero applied field. (a) PSD map as a function of current. The inset shows the measured spectrum at I = −15 mA with 5 visible harmonics. (b) Linewidth of the strongest (second) harmonic as a function of current, showing values as low as 6 MHz.

half-Heusler material NiMnSb. On the one hand, the Py-based devices have high repeatability and show hysteretic oscillations that can be attributed to vortex/antivortex generation and annihilation. Details of this work can be found in manuscript **II**. On the other hand, a signature of the NiMnSb-based devices is their low linewidth and low threshold current, though they suffer from low repeatability. Details of this work can be found in manuscript **III**.

2.1 Py-Based Single-Layer NC-STOs

The material stack of these devices consists of a 5 nm Pd seed layer, a 20 nm Cu bottom electrode, a 7.7 nm single Py layer, and a Cu (2 nm)/Pd(2 nm) capping layer, as shown in Fig. 2.1(b). The NCs studied here have a nominal diameter of 100 nm etched into a 30 nm thick insulation layer of SiO_2. The current flow in NC-STOs is schematically indicated in Fig. 2.1(b), from which it is obvious that a larger current density, and therefore STT, is expected at the top Cu-Py interface than at the bottom Py-Cu interface. This in turn yields a net torque on the Py layer underneath the NC, which according to Ref. [61] results in antidamping in the case of electrons flowing from the top Cu layer into the Py layer. This is confirmed by our electrical measurements, where oscillation dynamics are only observed for negative applied currents.

The measurement scheme in these devices accounts for the strong current hysteresis observed, where first a current sweep is performed from 2 mA to −35 mA, followed by a sweep back from −35 mA to 2 mA. The small positive currents are applied to compensate for any remaining static magnetization configurations. A measurement at zero applied field is shown in Fig. 2.2, and it can be seen that at an onset current of −32 mA, a broad background signal emerges in the measured spectra. When sweeping the applied current back, the electrical signal changes into a distinct narrow-linewidth oscillation, decreasing in frequency from ≈3 GHz at a current of −34 mA to 250 MHz at −13 mA, below which no further signals are detected. For low applied currents, up to 5 harmonics of a fundamental frequency are observable, with the even

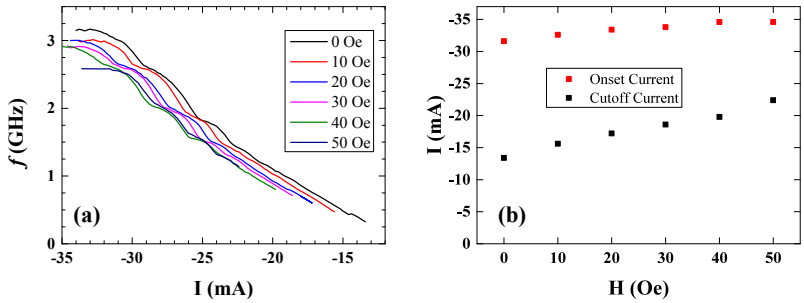

Figure 2.3: (a) Microwave emission frequency as a function of the bias current under small in-plane fields. The frequencies are smaller for larger applied fields. No signals are observed above 50 Oe. (b) The onset currents and cutoff currents as a function of the applied field. The dynamics are sustained for the largest range of currents at zero applied field.

harmonics being stronger than the odd ones, showing the high nonlinearity of the spin-wave modes [102].

The influence of a small in-plane field along the direction of the mesa [see Fig. 2.1(a)] is then studied in more detail, and is shown in Fig. 2.3. It is observed that it has a negative effect on the oscillation dynamics, since higher currents are needed to nucleate the initial broadband dynamics, and the oscillations do not remain until the same low currents as is the case for zero-field operation. The dependence of onset current and cutoff current shows a linear trend with the in-plane field; see Fig. 2.3(b). For fields larger than 50 Oe, the current of $-35\,\mathrm{mA}$, which is the maximum current the devices can sustain for a long time, is no longer sufficient to excite dynamics. Contrary to what one would generally expect for spin-wave frequencies, the frequency of the oscillations reduces with a larger applied magnetic field.

From the strong hysteretic behavior of the microwave emission, it can be reasoned that the physical origin is related to vortex dynamics [103]. Such magnetic vortices are stable circular structures in extended films that can be nucleated by, for example, the Oersted field from the current in the nanocontact [104]. However, our signals cannot be directly related to the most common type of STT-induced excitation, the vortex gyration, which describes the movement of the vortex core underneath the NC [105, 106]. Compared to the signals from vortex gyrations, our devices show an unusually high frequency and a much higher current tunability ($\approx$160 MHz/mA) than expected.

It has recently been shown in micromagnetic simulations [107, 108] that the periodic creation and annihilation of small vortex–antivortex pairs underneath the NC can result in a similar linear increase in the frequency with the bias current as is observed in our devices. This is due to the linearly increasing energy potential from the current-generated Oersted field. A small external in-plane field will also alter this potential landscape by adding a tilt to it, which can in turn reduce its effective height and therefore lead to reduced oscillation frequencies, as seen in our study.

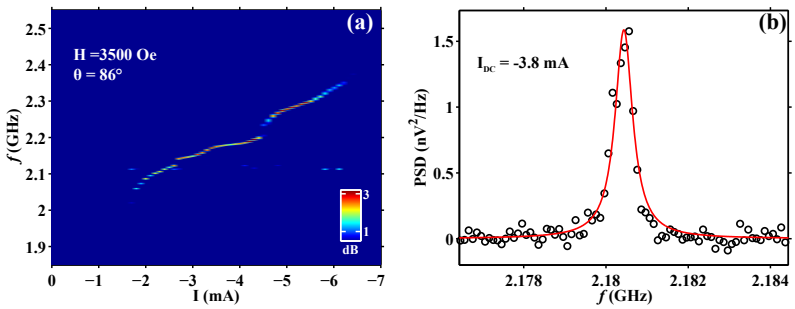

Figure 2.4: Microwave emission of single-layer NC-STO with a 30 nm thick NiMnSb layer. (a) PSD map as a function of bias current, showing a threshold of $I_{th} = -1.9\,\mathrm{mA}$. (b) Measurement of a single spectrum at $I = -3.8\,\mathrm{mA}$. The red solid line is a Lorentzian fit to the spectrum, yielding an FWHM of 520 kHz

2.2 NiMnSb-Based Single-Layer NC-STOs

The successful observation of electrical microwave signals in permalloy-based single-layer NC-STOs motivates similar experiments on devices with a Heusler magnetization layer. Half-metallic Heusler materials, such as Co_2(Mn,Fe)Si and NiMnSb, are promising candidates for spintronic devices, due to their intrinsic low damping constants [109, 110] and high spin polarization at the Fermi level [111, 112, 113, 114]. Only recently, the half-metallic Heusler material Co_2(Mn,Fe)Si was employed in nanopillars [115, 116], as well as in nanocontact oscillators [117], showing high output power. This is achieved through the enhanced GMR effect stemming from the unusually high spin polarization. Here, we employ the half-Heusler material NiMnSb, which has a considerably lower damping constant than Co_2(Mn,Fe)Si in NC-STOs. Owing to the fact that the magnetodynamic properties of NiMnSb are superior when grown by molecular beam epitaxy (MBE) on InP(001) substrates [118, 119, 76], we are here initially limited to a single-layer of NiMnSb, rather than two layers separated by a metallic spacer.

The layer structure of the NC-STO is displayed in Fig. 2.1(c), where the Cu(1.5 nm) capping layer was deposited *in situ* after the growth of NiMnSb to protect the material from oxidation and relaxation. Auto-oscillations were observed in NC-STOs from 40 nm and 30 nm thick NiMnSb, without any noticeable difference in performance between them.

A measurement of an NC-STO from the 30-nm thick Heusler layer with a 90 nm diameter NC is shown in Fig. 2.4(a). The device has a typical dc resistance of $22.4\,\Omega$ at 1 mA, which is much higher than in permalloy-based NC-STOs and can be explained by the absence of a thick Cu bottom electrode. The magnetic field of 3500 Oe is oriented at an angle of 86° w.r.t. the sample plane. Under these conditions, the auto-oscillations are visible starting from a current of $I = -1.8\,\mathrm{mA}$, which results in an estimated threshold current density of $j_{th} \approx 3 \times 10^{11}\,\mathrm{A/m^2}$. This value is much lower than the values being

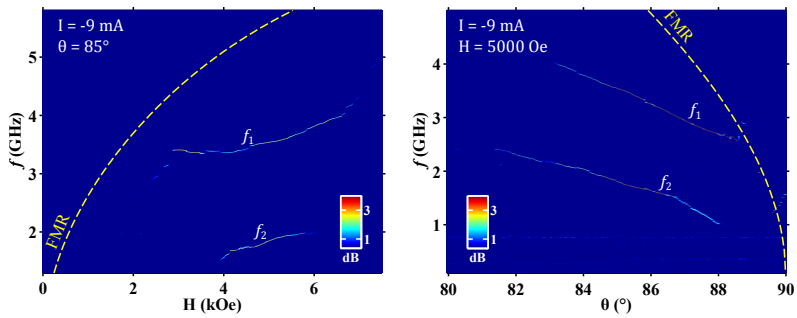

Figure 2.5: Microwave emission at constant current of I $= -9$ mA from a 90 nm point contact on top of a 40 nm thick NiMnSb layer. (a) PSD map as a function of applied field and (b) PSD map as a function of applied field angle θ. Two modes (f_1 and f_2), separated by $\approx$1.5 GHz, are observable. Under certain conditions, the frequencies $f_1 + f_2$ and $f_1 - f_2$ are also visible, proving intermodulation between the two modes.

reported for spin-valve NC-STOs of comparable contact sizes [120, 104, 121], whereas low thresholds are typically observed for vortex excitations. Besides the low threshold current, also the repeatedly observed low linewidth of the oscillations is remarkable. This is shown by the spectrum taken at a current of $I = -3.8$ mA in Fig. 2.4(b). The signal can be fit to a Lorentzian function with an FWHM of 520 kHz, which is about an order of magnitude less than the values achieved for permalloy-based NC-STOs [122]. This low linewidth is a direct consequence of the drastically lower intrinsic Gilbert damping of NiMnSb compared to Py.

In a number of the tested devices, it is also possible to observe two oscillation modes at the same time, despite the existence of only a single nanocontact, as is demonstrated in Fig. 2.5. These results originate from an NC-STO with a 90 nm diameter NC on top of the 40 nm NiMnSb film. The bias current of $I = -9$ mA is kept constant while the auto-oscillation spectra are recorded at different field strengths [Fig. 2.5(a)] or while changing the field angle by rotating the sample [Fig. 2.5(b)]. The FMR frequencies calculated from the magnetostatic boundary conditions are drawn in each figure, showing that the modes have a frequency well below FMR, as is observed for all auto-oscillations in these devices. However, in agreement with the general trend in STOs, the auto-oscillation frequencies increase with increasing field strength and decreasing out-of-plane angle. For all devices we measure an insufficiently low integrated output power of $\leq$0.05 pW, which is due to the electrical read-out in single-layer devices relying on the AMR effect. However, this is comparatively small in NiMnSb [93].

The microscopic nature of the observed oscillations is not yet fully understood, partially on account of the fact that the repeatability between two nominally identical devices is relatively poor in terms of working range and frequencies. The parameters, field, and angle in Fig. 2.5 approximately describe

the overall conditions for which signals have been observed in roughly 60 % of the tested NiMnSb single-layer NC-STOs. However, while for some devices the field range spans only a couple of hundred Oe, some extend over a few thousand Oe. Signals have been not observed for fields larger than ≈8000 Oe, which is less than the saturation magnetization, and suggests the necessity of a nonhomogeneous magnetization in the relatively thick NiMnSb films. Moreover, the microwave signals are more likely to be present in a field tilted a few degrees away from the perpendicular direction, as can be seen in Fig. 2.5(b), where the stable two modes are observed only for angles below 88.5°. The fact that no significant differences in linewidth or current dependence are seen between devices from the 30 nm and 40 nm thick films is evidence that the auto-oscillations are of essentially superficial origin.

In previous studies on mechanical point contacts with single-layer ferromagnetic films at cryogenic temperatures, nanoscopic magnetic domains have appeared on the interface between the tip and the film. These can eventually form a spin valve with the bulk ferromagnetic layer [62, 123, 124, 125, 126]. Although the formation and physical layout of the nanodomain underneath the nonmagnetic tip material have not yet been fully explained in the literature, it may be possible to explain some of the observations with this kind of structure in our devices. Mainly, the device yield and the somewhat randomized results in terms of microwave excitation parameters have been observed in mechanical point contact systems [127, 128]. This is plausible, as these processes are sensitive to the exact parameters of point contact formation, which can be controlled only to a certain extent. For example, in our case of epitaxially grown films, the location of the NCs w.r.t. any surface defect could potentially have an influence. These defects can act as pinning sites for, for example, magnetic domains in the bulk film, and may be either intrinsic or introduced by our fabrication processes.

3

Magnetization Dynamics in Spin Hall Nano-Oscillators

This chapter will focus on the generation of microwave signals in SHNOs [36], under both in-plane and tilted applied magnetic fields. The first report of electrically measured high-frequency signals in SHNOs appeared in 2013 as Ref. [37]; the devices in this were operated with in-plane magnetic fields at cryogenic temperatures. While, for low temperatures, a stable low-linewidth (6 MHz) signal was measured, the oscillation characteristics changed dramatically towards higher temperatures with the appearance of a high-frequency mode with much larger linewidths, barely observable at room temperatures.

Here, only room-temperature measurements will be utilized. However, the signals obtained are larger than those of previous reports, presumably due to the possibility of measuring with less losses when not utilizing a cryostat. It will be shown which sample properties are important for the device characteristics, and the successful observation of SHE-induced dynamics will be shown for three different FM materials. A similar behavior to the case of cryogenic measurements, where two different modes have been observed, can then be established by simply introducing an out-of-plane tilt to the magnetic field. This is of technological importance, as the low-linewidth bullet mode can in this way be easily accessed at room temperature, and also can be tuned in a much broader frequency range than previously reported.

The devices described in this chapter each consist of a 4 µm diameter disk of FM/Pt bilayer. The current is localized to a nm-sized region with the help of sharp-tip Au electrodes that are centrally located on the disk and have spacings between the electrode tips from 50 nm to 300 nm. The studied FM materials are $Co_{40}Fe_{40}B_{20}$(5 nm) (manuscript **V**), NiMnSb(41 nm) (manuscript **IV**), NiMnSb(5 nm), and $Ni_{80}Fe_{20}$(5 nm) (manuscript **VI**). The last of these is shown here to have the highest electrical output power, which can be readily justified from the AMR ratios of these materials. However, the first two studies also serve as proofs-of-principle that the SHNO geometry is versatile and can be implemented in a variety of FM materials.

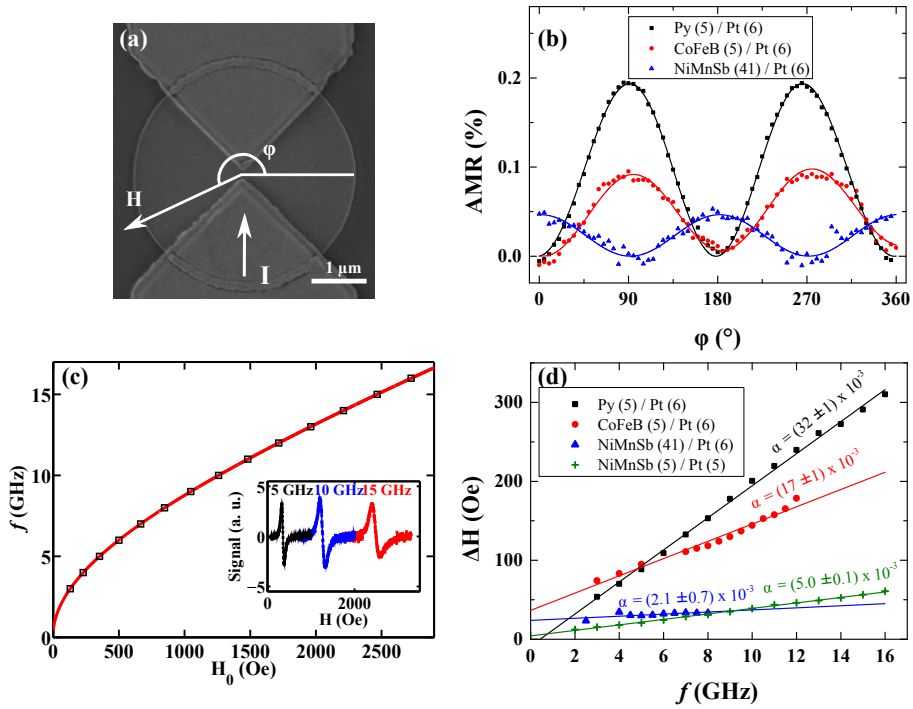

Figure 3.1: (a) SEM topview micrograph of the SHNO layout. The in-plane angle φ and the positive current direction are defined as shown in the picture. (b) Normalized AMR measurements with saturating in-plane fields of $\geq$500 Oe for the three films contained in the manuscripts. (c) FMR characterization of the Py (5 nm)/Pt (6 nm) bilayer. The solid line is a fit to the Kittel equation. The inset shows FMR data for 5 GHz, 10 GHz and 15 GHz. (d) Linear fits to the FMR linewidths yield the damping constant of the bilayers, with the NiMnSb-based films clearly having the lowest damping.

3.1 Basic Film Characterizations

To relate the auto-oscillation characteristics of the devices made from various FM films, it is important to have an understanding of their basic magnetodynamic properties, such as their saturation magnetization M_0, damping α, and AMR.

The characterizing measurements for the three previously mentioned films are summarized in Fig. 3.1. The AMR of the bilayer can be directly related to the magnitude of any of the obtained electrical signal, such as in ST-FMR and microwave emission measurements. The AMR measurements in Fig. 3.1(b) were carried out on the final devices, where a rotating in-plane field is provided by a projected field magnet. The magnitude of the field is $\geq$500 Oe for all measurements, which is large enough to ensure that the magnetization in the device follows the direction of the applied field. The solid lines in the

figure are fits to eq. 1.2. For thin Py films, AMR ratios of ≈3 % are available in the literature [55]. The much lower measured ratio of (0.19 ± 0.01) % is evidence that most of the current is shunted by the Pt(6 nm)-layer in the bilayer, due to its much higher conductivity. On one hand, this high current flow in Pt is desired, as it generates the necessary transverse spin currents to excite the magnetodynamics, but on the other hand, it reduces the possible amplitude of the measured electrical signal by more than an order of magnitude. The successful operation of SHNOs therefore depends to a certain extent on balancing the thicknesses of the FM and NM layers to achieve the necessary current densities, as well as on the AMR ratio of the FM layer itself. One prime example of this is the NiMnSb(41 nm)/Pt(6 nm) bilayer, where we measure a considerable AMR of (-0.04 ± 0.01) %, but only achieve this by increasing the thickness of the NM layer. This reduces the current density in Pt to such low values that no auto-oscillations can be observed. As a comparison, the AMR in devices made from NiMnSb(5 nm)/Pt(5 nm) (not shown) is reduced accordingly to (-0.007 ± 0.003) %, making it therefore barely possible to electrically observe signals.

Fig. 3.1(c) shows FMR data obtained from the extended bilayers—that is, prior to any device fabrication processes. M_0 and α, which can be determined from these measurements, have an important impact on the key values of oscillation frequency and linewidth, respectively. The measured FMR data [inset of Fig. 3.1(c)] is fit by eq. 1.7 to obtain the resonance fields and the linewidths. H_0 as a function of f_0 is then fit by the Kittel equation (eq. 1.5) and an effective magnetization of $\mu_0 M_{eff} = 0.79$ T for the Py film is obtained. The similarly obtained values for the $Co_{40}Fe_{40}B_{20}$ and NiMnSb films are 1.27 T and 0.72 T, respectively.

The FMR linewidth, as a function of f_0, is then fit by the linear function eq. 1.8—see Fig. 3.1(d). In this way, the damping of the Py (5 nm)/Pt (6 nm) bilayer is determined o to be 32×10^{-3}, which is more than three times the value for the pure Py thin films [129]. The Gilbert damping constants of $Co_{40}Fe_{40}B_{20}$ and NiMnSb are also significantly enhanced above their respective single-layer values [130, 131]. This can be explained by the spin-pumping effect [132, 133], as well as the magnetic proximity effect [134]. In the case of spin pumping, the energy of the magnetization precession in the FM is lost by a spin current directed into the adjacent NM metal—more significantly for materials with large spin-orbit interactions. Additionally, the Pt atoms at the NM/FM interface gain a magnetic moment, the magnetic proximity effect [135], which also leads to increased damping. Although a material with low damping is preferred for low threshold currents and low linewidth oscillations, these enhancements of the Gilbert damping must be accepted, and are present in all the studied bilayers. The intrinsic damping and the increase in the damping from the Pt layer are dependent on the thickness of the FM and NM layer, respectively, adding more constraints to the thicknesses in the bilayer for the engineering of working SHNOs.

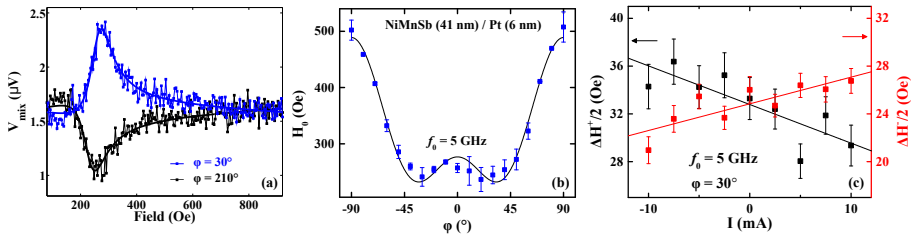

Figure 3.2: ST-FMR measurements NiMnSb(41 nm)/Pt(6 nm) SHNOs. (a) Mixing voltage as a function of applied field for two oppositely directed fields. The applied microwave current has a frequency of f=5 GHz and the data is fit to asymmetric Lorentzian functions. (b) The resonance fields obtained from the fits as a function of the applied field angle. The solid line is obtained by fitting the data with a biaxial and uniaxial in-plane anisotropy field. (c) When applying an additional bias current to the device, the ST-FMR linewidth decreases when field and current have the same sign, and increases for opposite signs.

3.2 Spin Hall Effect Controlled Magnetodynamics

The influence of the spin Hall effect on the magnetodynamic properties of the adjacent FM material can be directly shown by ST-FMR measurements (see also section 1.2.2). The application of an rf current leads to a periodic transverse spin current through the SHE which, in the resonance condition, yields a sizable dc voltage via the mixing of the rf current with the time-varying AMR of the same frequency. The data on the ST-FMR measurements on SHNOs from the NiMnSb(41 nm)/Pt(6 nm) bilayer is pictured in Fig. 3.2. Fig. 3.2(a) shows the mixing voltage as a function of the applied field, where the field is directed at angles of $\varphi = 30°$ and 210°—that is, along one axis but with opposite signs. The data can be fit with eq. 1.9, where the symmetric Lorentzian part is related to the SHE-induced spin torque. As can be expected for these bilayer films, the sign of the symmetric Lorentzian part changes when the direction of the magnetic field is reversed [66]. As can also be easily seen, the resonance field does not change when the direction of the magnetic field is reversed.

Epitaxially grown NiMnSb films experience a unique in-plane anisotropy, with a strong uniaxial anisotropy term along the [110] or [1$\bar{1}$0] crystallographic direction and a weaker biaxial anisotropy along the [100] and [010] directions [76]. The anisotropy energy densities K_u and K_b, for the uniaxial and biaxial term, respectively, result in internal fields $\frac{2K_u}{M_0}$ and $\frac{2K_b}{M_0}$, which can shift the resonance condition by several hundred Oersted. This is naturally true for the fabricated SHNOs as well, as can be seen in Fig. 3.2(b), where the ST-FMR measurements have been conducted for in-plane field angles between $-90°$ and 90° with $\varphi = 0°$ being the [110] direction. The obtained

resonance fields can be fit well with the anisotropy fields of $\frac{2K_u}{M_0} = 130$ Oe and $\frac{2K_b}{M_0} = 70$ Oe, where [110] is the dominating uniaxial easy axis. This tunability of the resonance frequency with the field angle introduces a new parameter for tuning the output characteristics of SHNOs fabricated from NiMnSb.

The most important effect of the SHE in FM/NM bilayers is the constant antidamping induced by the spin current from the Pt layer. This can also be shown for the case of subthreshold currents by ST-FMR measurements, where an additional dc current is applied to the sample. As the SHE in the Pt layer follows the right-hand rule, the magnetic moment of the spin accumulation at the NiMnSb/Pt interface points towards $\varphi = 180°$ for positive currents and along 0° for negative currents. An effective spin-torque antidamping is expected according to eq. 1.3 when the spin-current polarization and the magnetization are antiparallel. It is therefore expected that, for positive fields between $-90°$ and 90°, a positive current leads to reduced damping in the FM layer and thus to a reduced FMR linewidth. The same effect is true for negative currents and opposite field directions, while an additional damping is expected for opposite polarities of current and field. It is possible to show this effect in our NiMnSb SHNOs by plotting the ST-FMR linewidth as a function of the applied current for two oppositely directed fields—that is, along 30° and 210°, as shown in Fig. 3.2(c). The linewidths show a linear decrease (increase) with positive (negative) bias currents. However, the reduction in the NiMnSb SHNOs is minute compared to Py/Pt bilayers [66], which can be explained by the great thickness of the NiMnSb(41 nm) and the concomitant reduction of the current density in Pt. Extrapolating the ST-FMR linewidth to 0 Oe—the condition at which auto-oscillations can be expected—yields currents on the order of 80 mA to 100 mA. However, this is beyond the breakdown point of the SHNOs, which occurs due to Joule heating, and no auto-oscillations can be expected for these devices.

3.3 In-Plane Field Auto-Oscillations

Due to the read-out of the auto-oscillations by the time-varying AMR, it is important to operate the devices with an applied field angle of $\varphi \neq 0°$. The apparent minimum or maximum at this angle [see Fig. 3.1(b)] leads to a vanishing change in the AMR during small-angle precessions, similar to what has been shown for the TMR read-out in MTJ-STOs [136]. The in-plane angles at which auto-oscillations are measured thus lie between 10° and 40°, which represents a balance between the AMR readout being maximum at 45° and the STT efficiency being maximum at 0°.

Fig. 3.3 shows electrical signals measured from SHNOs with three different materials: Py, $Co_{40}Fe_{40}B_{20}$, and NiMnSb, each of 5 nm thickness. The current dependence of the signals is comparable between all samples. The signals are only observable for a current range of ≈3 mA, with the amplitude (linewidth) having a maximum (minimum) in the center of this region. Besides this, the signals have a slight red-shift towards higher currents. The main differences between the three materials emerge in the frequency, signal am-

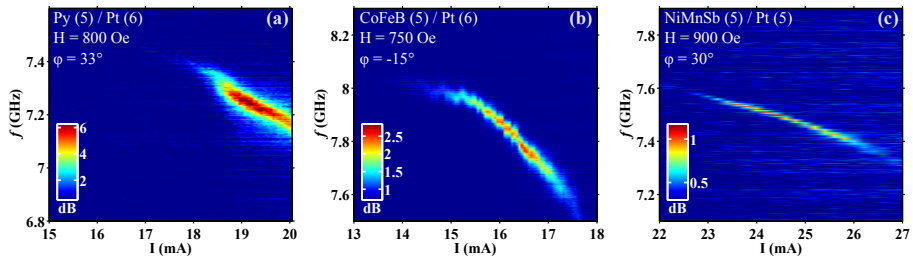

Figure 3.3: The electrically measured auto-oscillations of SHNOs from (a) Py (5 nm) (b) $Co_{40}Fe_{40}B_{20}$ (5 nm), and (c) NiMnSb (5 nm) films, where the measurements were taken at comparable in-plane applied fields. The axes in each figure span the same current and frequency intervals. While the output power is largest for (a), the linewidth is clearly lowest for (c).

plitude, linewidth, and threshold current, which can be all explained by the previously measured magnetodynamic properties.

On one hand, the maximum integrated powers of the measurements are 1.2 pW, 0.17 pW and 0.055 pW for the Py, $Co_{40}Fe_{40}B_{20}$, and NiMnSb devices, respectively, which obviously follows from the AMR of these three films. On the other hand, the respective minimum linewidths are 52 MHz, 41 MHz and 9.3 MHz, which is a direct consequence of the Gilbert damping constant. This decrease in linewidth to less than one fifth of the values achievable with permalloy shows once more the tremendous advantage of employing a low-damping material in spintronic oscillators. The current needed to operate the devices is lowest for the CoFeB film and highest for the NiMnSb-based devices, which can be related to the order of the electrical conductivities σ of the FM materials $\sigma_{Co_{40}Fe_{40}B_{20}} < \sigma_{Ni_{80}Fe_{20}} < \sigma_{NiMnSb}$ and to the therefore decreasing current density in the Pt layer.

The microwave frequencies for in-plane fields are in all cases observed between 300 MHz to 500 MHz below the respective FMR frequency of the extended film. As a result of this, the frequency of the CoFeB SHNO in Fig. 3.3 is highest, although it was measured at the lowest field due to its considerably larger saturation magnetization M_0. To understand both this difference from the FMR frequency and the red-shift with applied current, it avails to look into the Oersted field, which is the magnetic field generated by the current flow in the devices. Calculations of the current flow and the accompanying Oersted field are carried out using COMSOL Multiphysics® simulation software with a three-dimensional finite-element model of the device. Since the current in the device center is almost exclusively flowing along the y-axis, the x-component of the Oersted field is the most relevant one.

Fig. 3.4 shows the result for a Py (5 nm)/Pt (6 nm) SHNO containing 150 nm thick Au electrodes with a tip-to-tip spacing of 120 nm. In this model, the Oersted field H_{Oe} in the Py layer at the center of the disk is estimated to be 94 Oe in the negative $\hat{x}$ direction for a bias current of 20 mA, thus effectively reducing the externally applied field H. This reduction of the external field

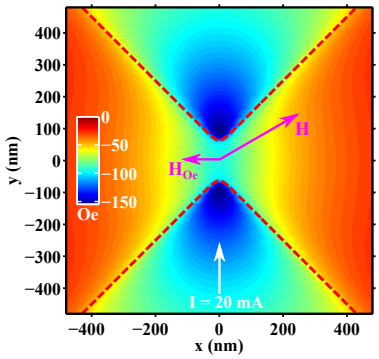

Figure 3.4: COMSOL simulation of the current-induced Oersted field (x-component) in the Py layer in a Py (5 nm)/Pt (6 nm)-based SHNO. The red dashed lines mark the location of the sharp-tip Au electrodes. The field is simulated for an applied current of I = 20 mA and reaches a value of -94 Oe in the center of the disk.

leads in turn to a shift in the local FMR frequency by several hundred MHz, depending on the angle of the applied field. Similar results can be obtained for the other bilayers, with the Oersted field being larger the more current flowing through the Pt—that is, in the case of high resistive FM materials. It can also be seen from Fig. 3.4 that the Oersted-field-induced reduction and thus the red-shift in frequency is larger the closer the in-plane angle lies to 0°, which is corroborated by the frequency tunability in the current scans at slightly different in-plane angles in Fig. 3.3. It can therefore be argued that the frequency of the observed auto-oscillations is solely the local FMR frequency at the disk center, amplified by the SHE from the Pt layer, and localized at the disk center by the minimum in the inhomogeneous field landscape.

3.4 Spin Hall Oscillators in Oblique Magnetic Fields

It was previously shown for NC-STOs that the auto-oscillation modes for in-plane magnetization become localized, while propagating modes are observed for tilted magnetizations [64, 14]. However, to date, auto-oscillations in SHNOs have been experimentally studied only for in-plane applied magnetic fields, where consequentially only localized modes have been observed. A self-localized spin-wave bullet at room temperature was found via μ-BLS [36], while electrically only a higher frequency mode was detectable, but was localized due to the FMR landscape [37, 137]. The lack of information about the microwave emission of SHNOs in tilted magnetic fields will be filled in here, where we investigate only the Py (5 nm)/Pt (6 nm) SHNOs, on account of their superior output power. It is found that by tilting the magnetization, the SHNO can be reliably tuned to either excite the high-frequency mode localized

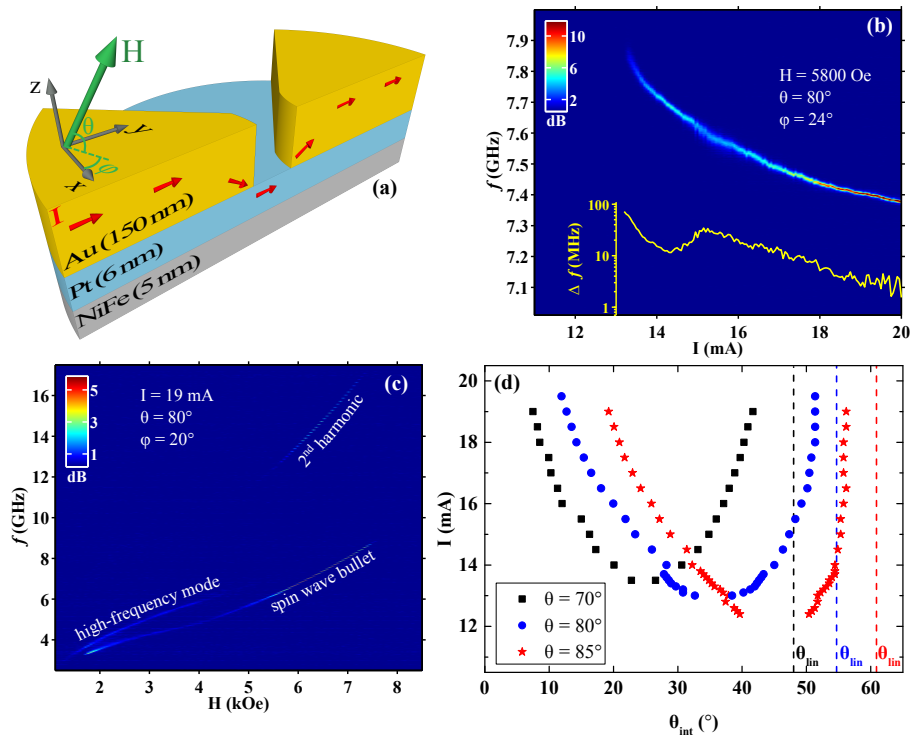

Figure 3.5: (a) Schematic of the SHNO device. The out-of plane angle θ is defined away from the film plane, as shown. (b) Microwave emission as a function of applied current for a device operated at $H = 5800$ Oe with $\theta = 80°$. Inset: The corresponding FWHM linewidth as obtained from Lorentzian fitting, showing an exponential decrease with a minimum value of 1.9 MHz. (c) Power spectral density as a function of applied field for a constant current of 19 mA showing the presence of two fundamentally different auto-oscillation modes. (d) The minimum and maximum *internal* magnetization angles at which the self-localized spin-wave bullet is observed.

by the Oersted field or the self-localized bullet mode; there are also many cases where both modes can be seen in the electrical spectra at the same time, suggesting a mode-coexistence or mode-hopping regime. Propagating spin-wave modes have not yet been observed experimentally in these tilted fields, although they are predicted to occur in perpendicularly magnetized fields from micromagnetic simulations [138].

Figure 3.5 shows information about the operation of the SHNO in oblique magnetic fields. The out-of-plane tilting angle θ of the external field is hereby defined additionally to the already introduced in-plane angle φ. A PSD map, as a function of the applied current, can be found in Fig. 3.5(b), where the applied field of 5800 Oe is directed along $\theta = 80°$ and $\varphi = 24°$. For these values of the field, we only observe the spin-wave bullet mode starting from a current of

$I = 13\,\mathrm{mA}$. It thus has a significantly lower threshold than the in-plane auto-oscillations [see Fig. 3.3(a)] and also stays present until the maximum applied current of 20 mA. The frequency shows a larger red-shift at the threshold, which is consistent with the decreasing size of the oscillation mode (*i.e.*, self-localization) [11, 12]. The measured linewidth thus drops exponentially from $\approx$80 MHz at the threshold to a minimum value of 1.9 MHz, seemingly only limited by the maximum applied current. This value is not only much lower than the high-frequency mode for in-plane fields, but is also lower than the previously reported values for the bullet mode at cryogenic temperatures [37, 137].

The microwave characteristics in tilted fields change drastically with the magnitude of the applied field, as can be seen from Fig. 3.5(c) for fields with $\theta = 80°$ and $\varphi = 24°$. In the low field region ($\leq$1700 Oe), only a weak signal of a high-frequency mode can be seen, which is shown to be of the same origin as the auto-oscillations for in-plane fields. This mode is stable only for fields up to $\approx$4000 Oe, above which it disappears. However, the spin-wave bullet appears above 1700 Oe and becomes clearly dominant in the absence of the high-frequency mode ($\geq$4000 Oe), where the bullet reaches the low linewidth and high peak power shown previously in Fig. 3.5(b). The occurrence of the second harmonic signal of the bullet in the high-field region is a direct sign of its large oscillation amplitude, as well as of its significant nonlinearity [102]. However, the characteristics of the spin-wave bullet in the intermediate region, where it is observed side-by-side with the high-frequency mode, are clearly compromised. This suggest a strong mode-coupling regime in which both modes interact through the transfer of magnons and thus equalize their power and linewidth [139, 140].

The minimum and maximum internal magnetization angles θ_{int}, between which the spin-wave bullet is observed, can be obtained from the minimum and maximum fields, respectively, through the magnetostatic boundary conditions (eq. 1.6). The critical angles θ_{int} are plotted in Fig. 3.5(d) as a function of the applied current for three different out-of-plane angles θ. It can be seen that the upper critical angle is monotonically increasing with the increasing tilt of the external field. To understand this upper boundary condition, it is helpful to calculate the nonlinear frequency shift N from the FMR properties [12]. The existence of a spin-wave bullet requires $N < 0$, which is only fulfilled for $\theta_{int} < \theta_{lin}$, at which θ_{lin} is the internal magnetization angle with $N = 0$. This critical angle is shown in the figure as dashed lines, and increases with increasing applied magnetic field angle in the same manner as observed in the electrical measurement. Above θ_{lin}, only linear propagating spin-wave modes can exist; presumably, however, with a higher threshold current than our current devices are able to handle. A lower critical angle is not predicted by the theory of Refs. [11, 12], where the bullet is the predominant mode for in-plane angles. However, the small θ_{int} in our experiment is accompanied by the occurrence of the high-frequency mode, leading to an effective lower critical angle of the spin-wave bullet due to competition between the two modes.

4

Mutual Synchronization of Spin Hall Nano-Oscillators

Spin Hall nano-oscillators exhibit a high nonlinearity, comparable to NC-STOs, as demonstrated by the existence of the spin-wave bullet in the previous chapter. This nonlinearity has already been used to readily phase-lock SHNOs to an external microwave current [141]. However, it is also known to promote the mutual synchronization of several oscillators; this has been demonstrated for up to three parallel NC-STOs sharing one free layer [23, 22, 142, 24]. While NC-STOs are mutually synchronized via the propagation of spin waves [143], SHNOs must face limitations coming from the spin-wave bullet mode with its self-localizing nature, hindering the interactions between oscillators.

In this chapter, the mutual synchronization of SHNOs based on Au electrodes on an extended film, as well as the synchronization of nanoconstriction based SHNOs, will be targeted. The successful mutual synchronization in both layouts is shown. The synchronization of needle SHNOs has many similarities to the case of NC-STOs, such as the parallel arrangement of two individual devices on one extended free layer, which leads to an increase in the current needed to drive both closely spaced SHNOs. This additional current substantially increases the Joule heating and thus limits the applicability of this scheme, especially when synchronizing a large number of devices.

However, due to the absence of an extended free layer in *nanoconstriction* SHNOs, these devices can be readily arranged in series [144, 145, 146, 147], with all oscillators sharing the same current path. Aside from the shared current, the nanoconstrictions are coupled through spin waves in the magnetic material in between, meaning that more robust synchronization is obtained in nanoconstriction SHNOs. In manuscript **VII**, the synchronization of two nanoconstrictions with distances of up to 1.2 µm, as well as of up to nine closer-spaced nanoconstrictions, is demonstrated. This number of synchronized devices is three times higher than the maximum reported number in NC-STOs [24]. The peak power density ($2700\,\mathrm{nV^2/Hz}$) and the quality factor (>10,000) of the nine synchronized SHNOs are about two orders of magnitude larger than values for single SHNOs [37].

4.1 Synchronization of Au Electrode SHNOs

As a logical step forward from SHNOs with a pair of sharp-tip Au electrodes, devices with double tips in the center of the extended disk are fabricated; see Fig. 4.1(a). To ensure that the pointed electrodes act as two independent SHNOs, it is important to increase the spacing between both electrode gaps to more than the gap distance. Otherwise, the current distribution in the Pt layer would readily merge into a single current path in the center. Additionally, double-needle SHNOs with large spacings between the electrodes have a higher yield in the lift-off process during fabrication, and will be therefore investigated here.

The device measured in Fig. 4.1 employs a double-tip with a distance of

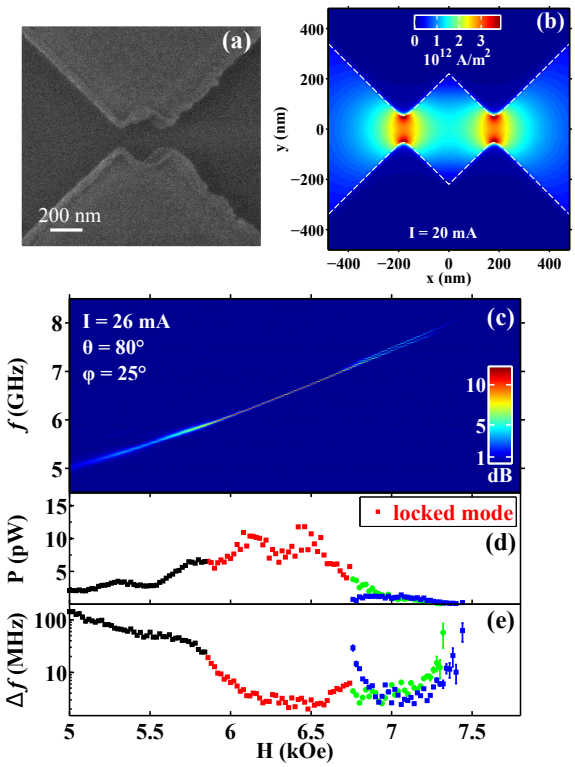

Figure 4.1: (a) SEM micrograph of an SHNO with two parallel Au electrode tips. (b) The simulated lateral current distribution (y-component) in the Pt layer. The current density between the two SHNOs drops to about 50 % of the value between the Au electrodes. (c) PSD map as a function of magnetic field for a constant current of I = 26 mA. The corresponding (d) integrated power and (e) linewidth suggest mutual synchronization between 5800 Oe and 6800 Oe due to a sharp increase of the output power and a decrease of the oscillation linewidth.

360 nm between the SHNOs, whose gap distances are 100 nm each. The expected current distribution for this geometry is shown in Fig. 4.1(b) and was calculated using COMSOL Multiphysics® software, ensuring that the requirement of two separated current paths in the device is fulfilled. The microwave emission characteristics of the device are summarized in Figs. 4.1(c-e), where the field magnitude is swept along $\theta = 80°$ and $\varphi = 25°$, keeping the current constant at I = 26 mA. While for fields ≥6800 Oe, two oscillation peaks from the two SHNOs can be observed, only one mode is measured between 5800 Oe and 6800 Oe, accompanied by a sharp increase in the power and linewidth as obtained from the Lorentzian fit. Although the expected spin-wave bullets in this field range are self-localizing, mutual synchronization is at least possible over a distance much larger than the extent of the bullet. This can be achieved either by dipolar interactions or by a small amount of evanescent spin waves from the bullets.

4.2 Synchronization of Nanoconstriction SHNOs

In the second possible SHNO layout, the current is focused on a nm-sized region by a constriction in the NM/FM bilayer [89]. The auto-oscillation characteristics are comparable to the Au electrode-based SHNOs in the sense that in-plane fields lead to relatively broad signals and a clear spin-wave bullet with low linewidth is formed only in tilted magnetic fields. Due to the absence of the extended magnetic free layer, the nanoconstriction SHNOs require far less current for oscillations. With the high-frequency mode having its origin in the extended magnetic film, it is also less pronounced in constriction-based SHNOs, giving way to the existence of spin-wave bullets for a wide range of applied fields.

While microwave signals in Au needle SHNOs show an exclusive dependence of lower frequencies on higher currents (red shift)—see Fig. 3.5(b)—the

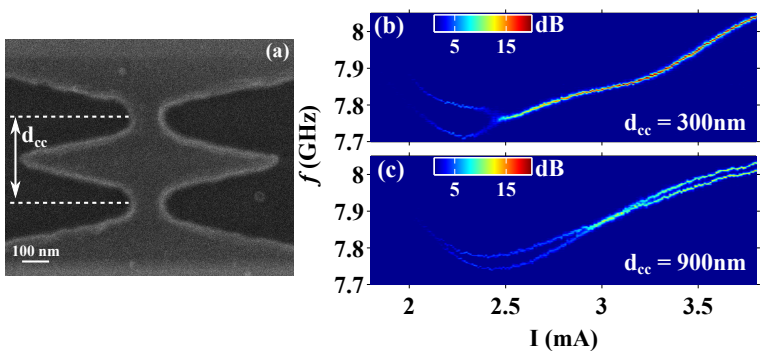

Figure 4.2: (a) SEM micrograph of two 120 nm wide nanoconstrictions, spaced d_{cc} = 300 nm apart. (b) and (c) PSD maps as a function of applied current for double nanoconstriction SHNOs with spacings of 300 nm and 900 nm, respectively.

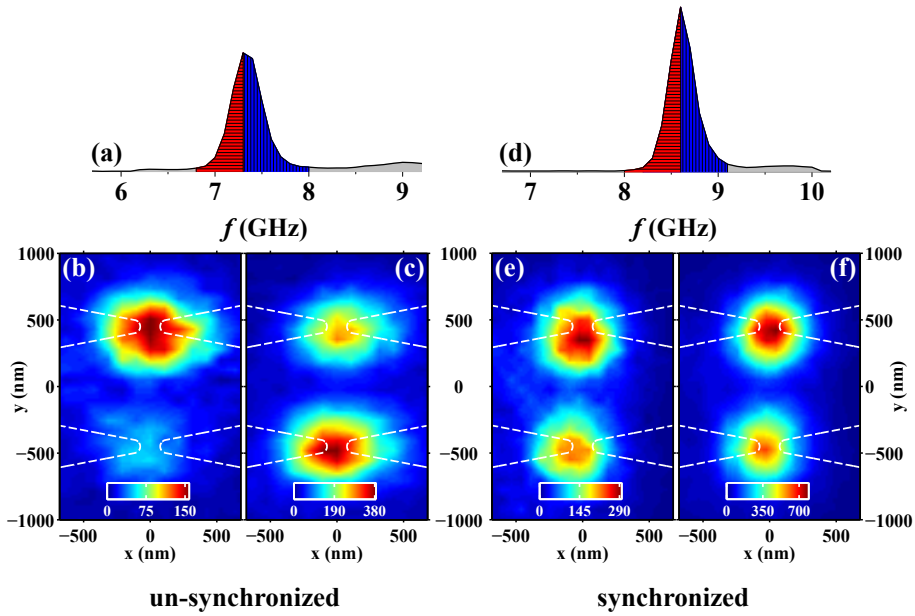

Figure 4.3: (a) Total μ-BLS spectrum in the unsynchronized state (I = 2.6 mA). (b) and (c) Spatial maps of the oscillation amplitude, focusing on the lower and upper frequency part of the total peak, respectively. (d)–(f) are the respective plots for the synchronized state at I = 3.0 mA. The positions of the constrictions are marked as white dashed lines

current dependence of the signal in constriction SHNOs is more complex. An initial red shift is followed by a turnover towards larger frequencies (blue shift), in which an increasing frequency with applied current is typically a sign of spin-wave propagation. The blue shift, in our case, can be related to the magnitude of the internal field, which results from the external field, the Oersted field, and an uniaxial in-plane anisotropy imposed by the shape of the constriction.

The microwave emission of two serially connected constrictions is described in Fig. 4.2. The spacing is varied here between 300 nm (see Fig. 4.2(a)) and 1.2 µm. Sample measurements as a function of the applied current are shown in Fig. 4.2(b) for double-constrictions with spacings of 300 nm and 900 nm. In all observed cases, successful synchronization of two constrictions is only possible for currents above the turnover point at ≈2.4 mA, where blue shifting of the signals begins. For the case of d_{cc} = 300 nm, Fig. 4.2(b), the signals from both constrictions merge into one oscillation peak with an increased output power and reduced linewidth at 2.5 mA. They remain synchronized up to the maximum applied current of 3.8 mA. As expected from a decreasing interaction with increasing oscillator distance [23], the mutual synchronization of constrictions with 900 nm spacing, Fig. 4.2(c), shows two oscillation peaks for most of the currents. Signs of mutual synchronization, such as frequency

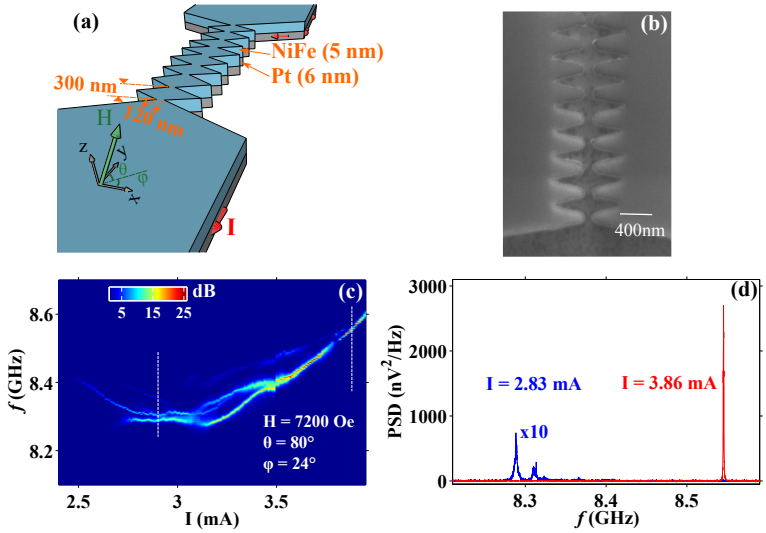

Figure 4.4: (a) Schematic and (b) SEM picture of the multinanoconstriction devices measured. (c) PSD as a function of applied current for an SHNO with 9 nanoconstrictions placed in series. The field of 7200 Oe is oriented in similar directions as for the previous SHNOs. (d) Plots of the PSD at the two currents of 2.83 mA and 3.86 mA. In the first case, only two constrictions are synchronized, while in the latter, all 9 constrictions show a single peak with a peak power density of 2700 nV^2/Hz.

pulling and merging of the two signals, can be found around 3 mA. However, with an increasing current, the frequency difference between the individual oscillators increases and the weak interaction is no longer sufficient for mutual synchronization.

Thanks to the optical access to the magnetization dynamics in SHNOs, the mutual synchronization of nanoconstrictions can be directly observed by μ-BLS measurements, as shown in Fig. 4.3. The device consists of two nanoconstrictions placed 900 nm apart. Due to the limited frequency resolution of the optical detection path, the total BLS signal appears as one single peak in both cases of unsynchronized [Fig. 4.3(a)] and synchronized [Fig. 4.3(d)] auto-oscillations. However, by dividing the μ-BLS map into the lower and higher frequency parts of the sum peak, one can immediately visualize the different behavior in the two cases. In the unsynchronized case in Figs. 4.3(b) and (c), the upper nanoconstriction is energized at lower frequencies and the bottom constrictions at higher frequencies. When both constrictions are synchronized (see Figs. 4.3(e) and (f)), they show no variation in their relative amplitude when focusing on the lower or higher frequency part of the BLS signals.

The remarkably robust synchronization of two 300 nm spaced nanoconstrictions encourages experiments involving the synchronization of a larger number of oscillators. The results from a device with 9 serially arranged

SHNOs are summarized in Fig 4.4. This is the maximum number of successfully synchronized devices achieved. Fig 4.4(c) shows a microwave emission measurement, where the current is swept up to 4 mA in a constant field of 7200 Oe along $\theta = 80°$ and $\varphi = 24°$. At low currents, the individual nanoconstrictions generate separate microwave signals. As more of the nanoconstrictions pass their minimum frequency, their mutual synchronization begins as pairwise synchronization and increases to regions where most (but not all) constrictions are mutually synchronized. In Fig 4.4(d), the PSD at 2.83 mA is displayed as a blue curve, where at least two constrictions have synchronized, alongside other, weaker signals from unsynchronized nanoconstrictions. At a current of 3.86 mA, it is, however, possible to observe a single high-power microwave peak with a linewidth of about 814 kHz and a peak power density of 2700 $\mathrm{nV^2/Hz}$, which is shown as a red curve in Fig 4.4(d). This suggests the full synchronization of all nine nanoconstrictions under these conditions.

Summary and Outlook

This thesis presents several experimental approaches to improving the key parameters of spin-torque oscillators, such as ease of fabrication, low current oscillations, and low linewidth signals with appreciable high powers and frequencies.

From the point of fabrication, all device layouts here can be processed with standard lithographical methods, and can possibly thus be integrated into current semiconductor-based technologies. The number of processing steps required for a working oscillator is clearly the lowest for nanoconstriction SHNOs, yet these offer the same or better electrical signal quality as compared to NC-STOs or SHNOs with an extended free layer. This makes constriction-based SHNOs likely to be the devices with the largest future potential, as was also shown by the mutual synchronization of several nanoconstrictions yielding high quality-factor signals.

The implementation of the low-damping material NiMnSb in Chapters 2 and 3 has led to low-linewidth signals at low threshold currents in NC-STOs, as well as low-linewidth auto-oscillations in SHNOs. However, given that Heusler materials generally possess lower AMR than permalloy, the present readout mechanism is limited and yields only low power signals. Overcoming this limitation by developing new readout schemes, such as an additional MTJ nanopillar on top of a NiMnSb SHNO, would greatly improve the power while maintaining the advantages of very low linewidth signals.

While in the case of NC-STOs, a current flow through the magnetic layer is required, the newer type of spin Hall nano-oscillators work on the basis of pure spin currents, making them more versatile and also somewhat easier to fabricate. Successful operation of SHNOs was shown for three different FM materials in Chapter 3. In the future, the two layouts of Au electrodes and nanoconstrictions for SHE-driven auto-oscillations are expected to be readily applicable to a much larger variety of materials.

It was shown in Chapter 3 that, with the application of out-of-plane magnetic fields, the electrical output characteristics of SHNOs can be drastically improved compared to in-plane fields and also compared to NC-STOs. This is achieved through the robust formation of a nonlinear self-localizing spin-wave bullet. Although numerically predicted [138], the experimental observation of propagating spin waves emitted from SHNOs remains an open problem, and will be an important step forward for the applicability of these devices in spin-wave based computing [18, 148, 149].

The mutual synchronization, as observed for two different SHNO layouts in Chapter 4, is crucial for meeting the power and phase-noise requirements

of commercial applications. Moreover, the demonstration of robust synchronization over large distances and a large number of nanoconstriction devices opens up additional intriguing possibilities in spin-wave-based computing—among other applications. While the mutual synchronization of nanoconstrictions was shown here with all devices connected on a line, one can envision more complex arrangements, such as spin-wave majority gates [150].

The limitations on the number of synchronized devices in the scheme presented here include the increasing distance between the first and last constriction, as well as the increasing electrical resistance, yielding larger Joule heating for each additional SHNO. However, these problems could be mitigated in the future by layout miniaturization or layer thickness optimizations, potentially allowing for smaller distances as well as generally lower currents needed for successful operation.

Appendix

A

Selected Lithography Recipes

A.1 Recipe for Photolithographic Lift-Off

- Spin-coat sample with lift-off resist:
  - LOR1A at 4000 min^{-1} for 1 min: results in $\approx$ 100 nm thickness. Appropriate for thin films, *e.g.*, alignment marks.
  - or LOR3A at 1700 min^{-1} for 1 min: results in $\approx$ 500 nm thickness. Appropriate for thicker films, *e.g.*, top contacts.
- Bake the lift-off resist on a hotplate at 160 °C for 5 min.
- Spin-coat photoresist Microposit S1813 at 4000 min^{-1} for 1 min: results in $\approx$ 1.3 µm thickness.
- Bake the sample on a hotplate at 115 °C for 2 min.
- Expose layout in the Suss MA/BA 6 contact mask aligner for 6.5 s (nominal UV light intensity: 6 $\mathrm{mW\,cm}^{-2}$).
- Develop in Microposit MF-319 Developer for 100 s. Rinse in DI-H_2O. Blow dry.
- Deposition of desired metals in AJA Phase II sputtering system.
- Film lift-off:
  - Soak sample in resist remover mr-Rem 400 at 55 °C for at least 30 min,
  - Agitate until the film is completely removed by either pipette stream or ultrasonic,
  - (Optional) Rinse in isopropyl alcohol,
  - Rinse thoroughly in DI-H_2O,
  - Blow dry with nitrogen.

A.2 Recipe for SHNO Mesa Fabrication

- Spin-coat negative e-beam resist ma-N 2401 at 4000 min^{-1} for 1 min: results in $\approx$ 100 nm thickness.
- Bake the sample on a hotplate at 90 °C for 1 min.
- E-beam lithography with JEOL JBX-9300FS at 100 kV with base dose of 260 $\mathrm{mJ\,cm}^{-2}$.
- Develop in ma-D 525 Developer for 30 s + 30 s. Rinse in DI-H_2O. Blow dry.
- Ion beam etching in Oxford Ionfab 300 Plus. U_{beam}=500 V, U_{acc}=300 V, I_{beam}=60 mA, 25° tilting, and 10 min^{-1} rotation. Etching progress is monitored via SIMS.
- Resist removal:
  - O_2 plasma etch in PlasmaTherm BatchTop RIE at 50 W and 250 mTorr for 1 min
  - Soak sample in resist remover mr-Rem 400 at 55 °C for at least 10 min
  - (Optional) Agitate with ultrasonic
  - (Optional) Rinse in isopropyl alcohol
  - Rinse thoroughly in DI-H_2O
  - Blow dry with nitrogen

A.3 Recipe for Gold Electrode Fabrication

- Spin-coat positive e-beam resist SX ARP 6200/2 at 4000 min^{-1} for 1 min: results in $\approx$ 220 nm thickness.
- Bake the sample on a hotplate at 160 °C for 5 min.
- Deposition of 20 nm Cu in AJA Phase II sputtering system for discharge and optical reflection. (only for transparent and highly resistive substrates, *e.g.*, sapphire and GGG)
- E-beam lithography with JEOL JBX-9300FS at 100 kV with base dose of 380 $\mathrm{mJ\,cm}^{-2}$ (sapphire substrate) or 270 $\mathrm{mJ\,cm}^{-2}$ (InP substrate).
- Removal of the Cu discharge layer by wet etching in standard premixed Chromium etchant (water, ceric ammonium nitrate, nitric acid). Rinse with water. Blow dry.
- Develop in n-amyl acetate for 60 s. Blow dry.
- Deposition of 2 nm Cr + 150 nm Au in AJA Phase II sputtering system.

- Film lift-off:
  - Soak sample in resist remover mr-Rem 400 at 55 °C for at least 90 min,
  - Agitate until the film is completely removed by pipette stream,
  - (Optional) Rinse in isopropyl alcohol,
  - Rinse thoroughly in DI-H_2O,
  - Blow dry with nitrogen.

Bibliography

[1] S. A. Wolf, D. D. Awschalom, R. A. Buhrman, J. M. Daughton, S. von Molnár, M. L. Roukes, A. Y. Chtchelkanova, and D. M. Treger, "*Spintronics: A Spin-Based Electronics Vision for the Future*", Science **294**, 1488–1495 (2001).

[2] A. Fert, "*Nobel Lecture: Origin, development, and future of spintronics*", Rev. Mod. Phys. **80**, 1517–1530 (2008).

[3] V. V. Kruglyak, S. O. Demokritov, and D. Grundler, "*Magnonics*", J. Phys. D: Appl. Phys. **43**, 264001 (2010).

[4] S. O. Demokritov and A. N. Slavin, eds., *Magnonics - From Fundamentals to Applications* (Springer-Verlag Berlin Heidelberg, 2013).

[5] L. Berger, "*Emission of spin waves by a magnetic multilayer traversed by a current*", Phys. Rev. B **54**, 9353–9358 (1996).

[6] J. C. Slonczewski, "*Current-driven excitation of magnetic multilayers*", J. Magn. Magn. Mater. **159**, L1–L7 (1996).

[7] J. Slonczewski, "*Excitation of spin waves by an electric current*", J. Magn. Magn. Mater. **195**, 261–268 (1999).

[8] S. Bonetti, V. Tiberkevich, G. Consolo, G. Finocchio, P. Muduli, F. Mancoff, A. Slavin, and J. Åkerman, "*Experimental Evidence of Self-Localized and Propagating Spin Wave Modes in Obliquely Magnetized Current-Driven Nanocontacts*", Phys. Rev. Lett. **105**, 217204 (2010).

[9] S. Bonetti, V. Puliafito, G. Consolo, V. S. Tiberkevich, A. N. Slavin, and J. Åkerman, "*Power and linewidth of propagating and localized modes in nanocontact spin-torque oscillators*", Phys. Rev. B **85**, 174427 (2012).

[10] M. Madami, S. Bonetti, G. Consolo, S. Tacchi, G. Carlotti, G. Gubbiotti, F. B. Mancoff, M. A. Yar, and J. Åkerman, "*Direct observation of a propagating spin wave induced by spin-transfer torque*", Nature Nanotech. **6**, 635–638 (2011).

[11] A. Slavin and V. Tiberkevich, "*Spin Wave Mode Excited by Spin-Polarized Current in a Magnetic Nanocontact is a Standing Self-Localized Wave Bullet*", Phys. Rev. Lett. **95**, 237201 (2005).

[12] G. Gerhart, E. Bankowski, G. A. Melkov, V. S. Tiberkevich, and A. N. Slavin, "*Angular dependence of the microwave-generation threshold in a nanoscale spin-torque oscillator*", Phys. Rev. B **76**, 024437 (2007).

[13] V. E. Demidov, S. Urazhdin, and S. O. Demokritov, "*Direct observation and mapping of spin waves emitted by spin-torque nano-oscillators*", Nature Mater. **9**, 984–988 (2010).

[14] R. K. Dumas, E. Iacocca, S. Bonetti, S. R. Sani, S. M. Mohseni, A. Eklund, J. Persson, O. Heinonen, and J. Åkerman, "*Spin-Wave-Mode Coexistence on the Nanoscale: A Consequence of the Oersted-Field-Induced Asymmetric Energy Landscape*", Phys. Rev. Lett. **110**, 257202 (2013).

[15] M. A. Hoefer, T. J. Silva, and M. W. Keller, "*Theory for a dissipative droplet soliton excited by a spin torque nanocontact*", Phys. Rev. B **82**, 054432 (2010).

[16] S. M. Mohseni, S. R. Sani, J. Persson, T. N. A. Nguyen, S. Chung, Y. Pogoryelov, P. K. Muduli, E. Iacocca, A. Eklund, R. K. Dumas, S. Bonetti, A. Deac, M. A. Hoefer, and J. Åkerman, "*Spin Torque–Generated Magnetic Droplet Solitons*", Science **339**, 1295–1298 (2013).

[17] F. Macià, D. Backes, and A. D. Kent, "*Stable magnetic droplet solitons in spin-transfer nanocontacts*", Nature Nanotech. **9**, 992–996 (2014).

[18] A. Khitun, M. Bao, and K. L. Wang, "*Magnonic logic circuits*", J. Phys. D: Appl. Phys. **43**, 264005 (2010).

[19] B. Lenk, H. Ulrichs, F. Garbs, and M. Münzenberg, "*The building blocks of magnonics*", Phys. Rep. **507**, 107–136 (2011).

[20] A. V. Chumak, A. A. Serga, and B. Hillebrands, "*Magnon transistor for all-magnon data processing*", Nat. Commun. **5**, 4700 (2014).

[21] S. Urazhdin, V. E. Demidov, H. Ulrichs, T. Kendziorczyk, T. Kuhn, J. Leuthold, G. Wilde, and S. O. Demokritov, "*Nanomagnonic devices based on the spin-transfer torque*", Nature Nanotech. **9**, 509–513 (2014).

[22] S. Kaka, M. R. Pufall, W. H. Rippard, T. J. Silva, S. E. Russek, and J. A. Katine, "*Mutual phase-locking of microwave spin torque nano-oscillators*", Nature **437**, 389–392 (2005).

[23] F. B. Mancoff, N. D. Rizzo, B. N. Engel, and S. Tehrani, "*Phase-locking in double-point-contact spin-transfer devices*", Nature **437**, 393–395 (2005).

[24] S. Sani, J. Persson, S. Mohseni, Y. Pogoryelov, P. Muduli, A. Eklund, G. Malm, M. Käll, A. Dmitriev, and J. Åkerman, "*Mutually synchronized bottom-up multi-nanocontact spin-torque oscillators*", Nat. Commun. **4**, 2731 (2013).

[25] M. R. Pufall, W. H. Rippard, S. Kaka, T. J. Silva, and S. E. Russek, "*Frequency modulation of spin-transfer oscillators*", Appl. Phys. Lett. **86**, 082506 (2005).

[26] P. K. Muduli, Y. Pogoryelov, S. Bonetti, G. Consolo, F. Mancoff, and J. Åkerman, "*Nonlinear frequency and amplitude modulation of a nanocontact-based spin-torque oscillator*", Phys. Rev. B **81**, 140408 (2010).

[27] Y. Pogoryelov, P. K. Muduli, S. Bonetti, F. Mancoff, and J. Åkerman, "*Spin-torque oscillator linewidth narrowing under current modulation*", Appl. Phys. Lett. **98**, 192506 (2011).

[28] Y. Pogoryelov, P. K. Muduli, S. Bonetti, E. Iacocca, F. Mancoff, and J. Åkerman, "*Frequency modulation of spin torque oscillator pairs*", Appl. Phys. Lett. **98**, 192501 (2011).

[29] W. H. Rippard, M. R. Pufall, S. Kaka, T. J. Silva, S. E. Russek, and J. A. Katine, "*Injection Locking and Phase Control of Spin Transfer Nano-oscillators*", Phys. Rev. Lett. **95**, 067203 (2005).

[30] B. Georges, J. Grollier, M. Darques, V. Cros, C. Deranlot, B. Marcilhac, G. Faini, and A. Fert, "*Coupling Efficiency for Phase Locking of a Spin Transfer Nano-Oscillator to a Microwave Current*", Phys. Rev. Lett. **101**, 017201 (2008).

[31] S. Urazhdin, P. Tabor, V. Tiberkevich, and A. Slavin, "*Fractional Synchronization of Spin-Torque Nano-Oscillators*", Phys. Rev. Lett. **105**, 104101 (2010).

[32] S. Urazhdin, V. Tiberkevich, and A. Slavin, "*Parametric Excitation of a Magnetic Nanocontact by a Microwave Field*", Phys. Rev. Lett. **105**, 237204 (2010).

[33] P. Bortolotti, E. Grimaldi, A. Dussaux, J. Grollier, V. Cros, C. Serpico, K. Yakushiji, A. Fukushima, H. Kubota, R. Matsumoto, and S. Yuasa, "*Parametric excitation of magnetic vortex gyrations in spin-torque nano-oscillators*", Phys. Rev. B **88**, 174417 (2013).

[34] P. Dürrenfeld, E. Iacocca, J. Åkerman, and P. K. Muduli, "*Parametric excitation in a magnetic tunnel junction-based spin torque oscillator*", Appl. Phys. Lett. **104**, 052410 (2014).

[35] J. E. Hirsch, "*Spin Hall Effect*", Phys. Rev. Lett. **83**, 1834–1837 (1999).

[36] V. E. Demidov, S. Urazhdin, H. Ulrichs, V. Tiberkevich, A. Slavin, D. Baither, G. Schmitz, and S. O. Demokritov, "*Magnetic nano-oscillator driven by pure spin current*", Nature Mater. **11**, 1028–1031 (2012).

[37] R. H. Liu, W. L. Lim, and S. Urazhdin, "*Spectral Characteristics of the Microwave Emission by the Spin Hall Nano-Oscillator*", Phys. Rev. Lett. **110**, 147601 (2013).

[38] Z. Duan, A. Smith, L. Yang, B. Youngblood, J. Lindner, V. E. Demidov, S. O. Demokritov, and I. N. Krivorotov, "*Nanowire spin torque oscillator driven by spin orbit torques*", Nat. Commun. **5**, 5616 (2014).

[39] E. H. Hall, "*On a New Action of the Magnet on Electric Currents*", Amer. J. Math. **2**, 287–292 (1879).

[40] E. H. Hall, "*On the "Rotational Coefficient" in Nickel and Cobalt*", Proc. Phys. Soc. London **4**, 325 (1880).

[41] M. I. D'yakonov and V. I. Perel', "*Possibility of Orienting Electron Spins with Current*", JETP Lett. **13**, 467 (1971).

[42] Y. K. Kato, R. C. Myers, A. C. Gossard, and D. D. Awschalom, "*Observation of the Spin Hall Effect in Semiconductors*", Science **306**, 1910–1913 (2004).

[43] J. Wunderlich, B. Kaestner, J. Sinova, and T. Jungwirth, "*Experimental Observation of the Spin-Hall Effect in a Two-Dimensional Spin-Orbit Coupled Semiconductor System*", Phys. Rev. Lett. **94**, 047204 (2005).

[44] S. O. Valenzuela and M. Tinkham, "*Direct electronic measurement of the spin Hall effect*", Nature **442**, 176–179 (2006).

[45] A. Hoffmann, "*Spin Hall Effects in Metals*", IEEE Trans. Magn. **49**, 5172–5193 (2013).

[46] R. Karplus and J. M. Luttinger, "*Hall Effect in Ferromagnetics*", Phys. Rev. **95**, 1154–1160 (1954).

[47] J. Smit, "*The spontaneous hall effect in ferromagnetics II*", Physica **24**, 39–51 (1958).

[48] L. Berger, "*Side-Jump Mechanism for the Hall Effect of Ferromagnets*", Phys. Rev. B **2**, 4559–4566 (1970).

[49] S. Onoda, N. Sugimoto, and N. Nagaosa, "*Quantum transport theory of anomalous electric, thermoelectric, and thermal Hall effects in ferromagnets*", Phys. Rev. B **77**, 165103 (2008).

[50] C. Pai, L. Liu, Y. Li, H. W. Tseng, D. C. Ralph, and R. A. Buhrman, "*Spin transfer torque devices utilizing the giant spin Hall effect of tungsten*", Appl. Phys. Lett. **101**, 122404 (2012).

[51] G. Y. Guo, S. Murakami, T.-W. Chen, and N. Nagaosa, "*Intrinsic Spin Hall Effect in Platinum: First-Principles Calculations*", Phys. Rev. Lett. **100**, 096401 (2008).

[52] T. Tanaka, H. Kontani, M. Naito, T. Naito, D. S. Hirashima, K. Yamada, and J. Inoue, "*Intrinsic spin Hall effect and orbital Hall effect in 4d and 5d transition metals*", Phys. Rev. B **77**, 165117 (2008).

[53] H. Kontani, T. Tanaka, D. S. Hirashima, K. Yamada, and J. Inoue, "*Giant Orbital Hall Effect in Transition Metals: Origin of Large Spin and Anomalous Hall Effects*", Phys. Rev. Lett. **102**, 016601 (2009).

[54] W. Thomson, "*On the Electro-Dynamic Qualities of Metals:–Effects of Magnetization on the Electric Conductivity of Nickel and of Iron*", Proc. R. Soc. London **8**, 546–550 (1856).

[55] T. McGuire and R. Potter, "*Anisotropic magnetoresistance in ferromagnetic 3d alloys*", IEEE Trans. Magn. **11**, 1018–1038 (1975).

[56] F. J. Yang, Y. Sakuraba, S. Kokado, Y. Kota, A. Sakuma, and K. Takanashi, "*Anisotropic magnetoresistance in Co_2(Fe,Mn)Si Heusler epitaxial films: A fingerprint of half-metallicity*", Phys. Rev. B **86**, 020409 (2012).

[57] S. Kokado, M. Tsunoda, K. Harigaya, and A. Sakuma, "*Anisotropic Magnetoresistance Effects in Fe, Co, Ni, Fe_4N, and Half-Metallic Ferromagnet: A Systematic Analysis*", J. Phys. Soc. Jpn. **81**, 024705 (2012).

[58] A. Slavin and V. Tiberkevich, "*Nonlinear Auto-Oscillator Theory of Microwave Generation by Spin-Polarized Current*", IEEE Trans. Magn. **45**, 1875–1918 (2009).

[59] J. Nogués and I. K. Schuller, "*Exchange bias*", J. Magn. Magn. Mater. **192**, 203–232 (1999).

[60] P. C. van Son, H. van Kempen, and P. Wyder, "*Boundary Resistance of the Ferromagnetic-Nonferromagnetic Metal Interface*", Phys. Rev. Lett. **58**, 2271–2273 (1987).

[61] M. D. Stiles, J. Xiao, and A. Zangwill, "*Phenomenological theory of current-induced magnetization precession*", Phys. Rev. B **69**, 054408 (2004).

[62] Y. Ji, C. L. Chien, and M. D. Stiles, "*Current-Induced Spin-Wave Excitations in a Single Ferromagnetic Layer*", Phys. Rev. Lett. **90**, 106601 (2003).

[63] B. Özyilmaz and A. D. Kent, "*Current-induced switching in single ferromagenetic layer nanopillar junctions*", Appl. Phys. Lett. **88**, 162506 (2006).

[64] M. A. Hoefer, T. J. Silva, and M. D. Stiles, "*Model for a collimated spin-wave beam generated by a single-layer spin torque nanocontact*", Phys. Rev. B **77**, 144401 (2008).

[65] S. Sani, P. Dürrenfeld, S. Mohseni, S. Chung, and J. Åkerman, "*Microwave Signal Generation in Single-Layer Nano-Contact Spin Torque Oscillators*", IEEE Trans. Magn. **49**, 4331–4334 (2013).

[66] L. Liu, T. Moriyama, D. C. Ralph, and R. A. Buhrman, "*Spin-Torque Ferromagnetic Resonance Induced by the Spin Hall Effect*", Phys. Rev. Lett. **106**, 036601 (2011).

[67] V. E. Demidov, S. Urazhdin, E. R. J. Edwards, M. D. Stiles, R. D. McMichael, and S. O. Demokritov, "*Control of Magnetic Fluctuations by Spin Current*", Phys. Rev. Lett. **107**, 107204 (2011).

[68] L. Liu, O. J. Lee, T. J. Gudmundsen, D. C. Ralph, and R. A. Buhrman, "*Current-Induced Switching of Perpendicularly Magnetized Magnetic Layers Using Spin Torque from the Spin Hall Effect*", Phys. Rev. Lett. **109**, 096602 (2012).

[69] A. Hamadeh, O. d'Allivy Kelly, C. Hahn, H. Meley, R. Bernard, A. H. Molpeceres, V. V. Naletov, M. Viret, A. Anane, V. Cros, S. O. Demokritov, J. L. Prieto, M. Muñoz, G. de Loubens, and O. Klein, "*Full Control of the Spin-Wave Damping in a Magnetic Insulator Using Spin-Orbit Torque*", Phys. Rev. Lett. **113**, 197203 (2014).

[70] M. Collet, X. de Milly, O. d'Allivy Kelly, V. V. Naletov, R. Bernard, P. Bortolotti, V. E. Demidov, S. O. Demokritov, J. L. Prieto, M. Muñoz, V. Cros, A. Anane, G. de Loubens, and O. Klein, "*Generation of coherent spin-wave modes in Yttrium Iron Garnet microdiscs by spin-orbit torque*", arXiv:1504.01512 [cond-mat.mtrl-sci] (2015).

[71] L. Landau and E. Lifshits, "*On the theory of the dispersion of magnetic permeability in ferromagnetic bodies*", Phys. Zeitsch. der Sow. **8**, 153–169 (1935).

[72] C. Kittel, "*On the Theory of Ferromagnetic Resonance Absorption*", Phys. Rev. **73**, 155–161 (1948).

[73] C. Herring and C. Kittel, "*On the Theory of Spin Waves in Ferromagnetic Media*", Phys. Rev. **81**, 869–880 (1951).

[74] J. Coey, *Magnetism and Magnetic Materials* (Cambridge University Press, 2009).

[75] B. Heinrich, "*Radio Frequency Techniques*", in *Ultrathin Magnetic Structures II - Measurement Techniques and Novel Magnetic Properties*, edited by B. Heinrich and J. A. C. Bland (Springer Berlin Heidelberg, 1994).

[76] F. Gerhard, C. Schumacher, C. Gould, and L. W. Molenkamp, "*Control of the magnetic in-plane anisotropy in off-stoichiometric NiMnSb*", J. Appl. Phys. **115**, 094505 (2014).

[77] G. Woltersdorf, "Spin-pumping and two-magnon scattering in magnetic multilayers", PhD thesis (Simon Fraser University, 2004).

[78] N. Mecking, Y. S. Gui, and C.-M. Hu, "*Microwave photovoltage and photoresistance effects in ferromagnetic microstrips*", Phys. Rev. B **76**, 224430 (2007).

[79] S. O. Demokritov and B. Hillebrands, "*Spinwaves in Laterally Confined Magnetic Structures*", in *Spin Dynamics in Confined Magnetic Structures I*, edited by B. Hillebrands and K. Ounadjela (Springer Berlin Heidelberg, 2002).

[80] B. Lenk, G. Eilers, J. Hamrle, and M. Münzenberg, "*Spin-wave population in nickel after femtosecond laser pulse excitation*", Phys. Rev. B **82**, 134443 (2010).

[81] A. Conca, E. T. Papaioannou, S. Klingler, J. Greser, T. Sebastian, B. Leven, J. Lösch, and B. Hillebrands, "*Annealing influence on the Gilbert damping parameter and the exchange constant of CoFeB thin films*", Appl. Phys. Lett. **104**, 182407 (2014).

[82] S. S. Kalarickal, P. Krivosik, M. Wu, C. E. Patton, M. L. Schneider, P. Kabos, T. J. Silva, and J. P. Nibarger, "*Ferromagnetic resonance linewidth in metallic thin films: Comparison of measurement methods*", J. Appl. Phys. **99**, 093909 (2006).

[83] A. A. Tulapurkar, Y. Suzuki, A. Fukushima, H. Kubota, H. Maehara, K. Tsunekawa, D. D. Djayaprawira, N. Watanabe, and S. Yuasa, "*Spin-torque diode effect in magnetic tunnel junctions*", Nature **438**, 339–342 (2005).

[84] J. C. Sankey, P. M. Braganca, A. G. F. Garcia, I. N. Krivorotov, R. A. Buhrman, and D. C. Ralph, "*Spin-Transfer-Driven Ferromagnetic Resonance of Individual Nanomagnets*", Phys. Rev. Lett. **96**, 227601 (2006).

[85] J. N. Kupferschmidt, S. Adam, and P. W. Brouwer, "*Theory of the spin-torque-driven ferromagnetic resonance in a ferromagnet/normal-metal/ferromagnet structure*", Phys. Rev. B **74**, 134416 (2006).

[86] W. Chen, J.-M. L. Beaujour, G. de Loubens, A. D. Kent, and J. Z. Sun, "*Spin-torque driven ferromagnetic resonance of Co/Ni synthetic layers in spin valves*", Appl. Phys. Lett. **92**, 012507 (2008).

[87] O. Mosendz, J. E. Pearson, F. Y. Fradin, G. E. W. Bauer, S. D. Bader, and A. Hoffmann, "*Quantifying Spin Hall Angles from Spin Pumping: Experiments and Theory*", Phys. Rev. Lett. **104**, 046601 (2010).

[88] S. R. Sani, "Fabrication and Characterization of Nanocontact Spin-Torque Oscillators", PhD thesis (KTH - Royal Institute of Technology, 2013).

[89] V. E. Demidov, S. Urazhdin, A. Zholud, A. V. Sadovnikov, and S. O. Demokritov, "*Nanoconstriction-based spin-Hall nano-oscillator*", Appl. Phys. Lett. **105**, 172410 (2014).

[90] S. A. Campbell, *Fabrication Engineering at the Micro- and Nanoscale (3rd Edition)* (Oxford University Press, 2008).

[91] H. Elsner, H.-G. Meyer, A. Voigt, and G. Grützner, "*Evaluation of ma-N 2400 series DUV photoresist for electron beam exposure*", Microelectron. Eng. **46**, 389–392 (1999).

[92] H. Y. T. Nguyen, H. Yi, and K.-H. Shin, "*Using Electron-beam Resists as Ion Milling Mask for Fabrication of Spin Transfer Devices*", J. Magn. **12**, 12–16 (2007).

[93] P. Dürrenfeld, F. Gerhard, M. Ranjbar, C. Gould, L. W. Molenkamp, and J. Åkerman, "*Spin Hall effect-controlled magnetization dynamics in NiMnSb*", J. Appl. Phys. **117**, 17E103 (2015).

[94] M. A. Mohammad, M. Muhammad, S. K. Steven K. Dew, and M. Stepanova, "*Fundamentals of Electron Beam Exposure and Development*", in *Nanofabrication: Techniques and Principles*, edited by M. Stepanova and S. Dew (Springer-Verlag Wien, 2012).

[95] S. Bonetti, "Magnetization Dynamics in Nano-Contact Spin Torque Oscillators - Solitonic bullets and propagating spin waves", PhD thesis (KTH - Royal Institute of Technology, 2010).

[96] M. N. Baibich, J. M. Broto, A. Fert, F. N. Van Dau, F. Petroff, P. Etienne, G. Creuzet, A. Friederich, and J. Chazelas, "*Giant Magnetoresistance of (001)Fe/(001)Cr Magnetic Superlattices*", Phys. Rev. Lett. **61**, 2472–2475 (1988).

[97] G. Binasch, P. Grünberg, F. Saurenbach, and W. Zinn, "*Enhanced magnetoresistance in layered magnetic structures with antiferromagnetic interlayer exchange*", Phys. Rev. B **39**, 4828–4830 (1989).

[98] M. Julliere, "*Tunneling between ferromagnetic films*", Phys. Lett. A **54**, 225–226 (1975).

[99] I. K. Yanson, Y. G. Naidyuk, D. L. Bashlakov, V. V. Fisun, O. P. Balkashin, V. Korenivski, A. Konovalenko, and R. I. Shekhter, "*Spectroscopy of Phonons and Spin Torques in Magnetic Point Contacts*", Phys. Rev. Lett. **95**, 186602 (2005).

[100] B. Özyilmaz, A. D. Kent, J. Z. Sun, M. J. Rooks, and R. H. Koch, "*Current-Induced Excitations in Single Cobalt Ferromagnetic Layer Nanopillars*", Phys. Rev. Lett. **93**, 176604 (2004).

[101] S. Adam, M. L. Polianski, and P. W. Brouwer, "*Current-induced transverse spin-wave instability in thin ferromagnets: Beyond linear stability analysis*", Phys. Rev. B **73**, 024425 (2006).

[102] M. Quinsat, V. Tiberkevich, D. Gusakova, A. Slavin, J. Sierra, U. Ebels, L. Buda-Prejbeanu, B. Dieny, M.-C. Cyrille, A. Zelster, and J. Katine, "*Linewidth of higher harmonics in a nonisochronous autooscillator: Application to spin-torque nano-oscillators*", Phys. Rev. B **86**, 104418 (2012).

[103] M. R. Pufall, W. H. Rippard, M. L. Schneider, and S. E. Russek, "*Low-field current-hysteretic oscillations in spin-transfer nanocontacts*", Phys. Rev. B **75**, 140404 (2007).

[104] Q. Mistral, M. van Kampen, G. Hrkac, J. Kim, T. Devolder, P. Crozat, C. Chappert, L. Lagae, and T. Schrefl, "*Current-Driven Vortex Oscillations in Metallic Nanocontacts*", Phys. Rev. Lett. **100**, 257201 (2008).

[105] V. S. Pribiag, I. N. Krivorotov, G. D. Fuchs, P. M. Braganca, O. Ozatay, J. C. Sankey, D. C. Ralph, and R. A. Buhrman, "*Magnetic vortex oscillator driven by d.c. spin-polarized current*", Nature Phys. **3**, 498–503 (2007).

[106] M. Kammerer, M. Weigand, M. Curcic, M. Noske, M. Sproll, A. Vansteenkiste, B. Van Waeyenberge, H. Stoll, G. Woltersdorf, C. H. Back, and G. Schuetz, "*Magnetic vortex core reversal by excitation of spin waves*", Nat. Commun. **2**, 279 (2011).

[107] D. V. Berkov and N. L. Gorn, "*Non-linear magnetization dynamics in nanodevices induced by a spin-polarized current: micromagnetic simulation*", J. Phys. D: Appl. Phys. **41**, 164013 (2008).

[108] D. V. Berkov and N. L. Gorn, "*Spin-torque driven magnetization dynamics in a nanocontact setup for low external fields: Numerical simulation study*", Phys. Rev. B **80**, 064409 (2009).

[109] B. Heinrich, G. Woltersdorf, R. Urban, O. Mosendz, G. Schmidt, P. Bach, L. Molenkamp, and E. Rozenberg, "*Magnetic properties of NiMnSb(001) films grown on InGaAs/InP(001)*", J. Appl. Phys. **95**, 7462–7464 (2004).

[110] A. Koveshnikov, G. Woltersdorf, J. Q. Liu, B. Kardasz, O. Mosendz, B. Heinrich, K. L. Kavanagh, P. Bach, A. S. Bader, C. Schumacher, C. Rüster, C. Gould, G. Schmidt, L. W. Molenkamp, and C. Kumpf, "*Structural and magnetic properties of NiMnSb/InGaAs/InP(001)*", J. Appl. Phys. **97**, 073906 (2005).

[111] R. A. de Groot, F. M. Mueller, P. G. v. Engen, and K. H. J. Buschow, "*New Class of Materials: Half-Metallic Ferromagnets*", Phys. Rev. Lett. **50**, 2024–2027 (1983).

[112] D. Ristoiu, J. P. Nozières, C. N. Borca, T. Komesu, H.-k. Jeong, and P. A. Dowben, "*The surface composition and spin polarization of NiMnSb epitaxial thin films*", Europhys. Lett. **49**, 624 (2000).

[113] T. Kubota, S. Tsunegi, M. Oogane, S. Mizukami, T. Miyazaki, H. Naganuma, and Y. Ando, "*Half-metallicity and Gilbert damping constant in $Co_2Fe_xMn_{1-x}Si$ Heusler alloys depending on the film composition*", Appl. Phys. Lett. **94**, 122504 (2009).

[114] G. M. Müller, J. Walowski, M. Djordjevic, G. Miao, A. Gupta, A. V. Ramos, K. Gehrke, V. Moshnyaga, K. Samwer, J. Schmalhorst, A. Thomas, A. Hütten, G. Reiss, J. S. Moodera, and M. Münzenberg, "*Spin polarization in half-metals probed by femtosecond spin excitation*", Nature Mater. **8**, 56–61 (2009).

[115] R. Okura, Y. Sakuraba, T. Seki, K. Izumi, M. Mizuguchi, and K. Takanashi, "*High-power rf oscillation induced in half-metallic Co_2MnSi layer by spin-transfer torque*", Appl. Phys. Lett. **99**, 052510 (2011).

[116] T. Seki, H. Yako, T. Yamamoto, T. Kubota, Y. Sakuraba, M. Ueda, and K. Takanashi, "*Spin torque-induced magnetization dynamics in giant magnetoresistance devices with Heusler alloy layers*", J. Phys. D: Appl. Phys. **48**, 164010 (2015).

[117] T. Yamamoto, T. Seki, T. Kubota, H. Yako, and K. Takanashi, "*Zero-field spin torque oscillation in Co_2(Fe, Mn)Si with a point contact geometry*", Appl. Phys. Lett. **106**, 092406 (2015).

[118] P. Bach, A. S. Bader, C. Rüster, C. Gould, C. R. Becker, G. Schmidt, L. W. Molenkamp, W. Weigand, C. Kumpf, E. Umbach, R. Urban, G. Woltersdorf, and B. Heinrich, "*Molecular-beam epitaxy of the half-Heusler alloy NiMnSb on (In,Ga)As/InP (001)*", Appl. Phys. Lett. **83**, 521–523 (2003).

[119] P. Bach, C. Rüster, C. Gould, C. R. Becker, G. Schmidt, and L. W. Molenkamp, "*Growth of the half-Heusler alloy NiMnSb on (In,Ga)As/InP by molecular beam epitaxy*", Journal of Crystal Growth **251**, 323–326 (2003).

[120] W. Rippard, M. Pufall, S. Kaka, S. Russek, and T. Silva, "*Direct-Current Induced Dynamics in $Co_{90}Fe_{10}/Ni_{80}Fe_{20}$ Point Contacts*", Phys. Rev. Lett. **92**, 027201 (2004).

[121] M. Eggeling, T. Dimopoulos, T. Uhrmann, O. Bethge, R. Heer, V. Höink, and H. Brückl, "*Low spin current-driven dynamic excitations and metastability in spin-valve nanocontacts with unpinned artificial antiferromagnet*", Appl. Phys. Lett. **98**, 042504 (2011).

[122] S. Bonetti, P. Muduli, F. Mancoff, and J. Åkerman, "*Spin torque oscillator frequency versus magnetic field angle: The prospect of operation beyond 65 GHz*", Appl. Phys. Lett. **94**, 102507 (2009).

[123] T. Y. Chen, Y. Ji, C. L. Chien, and M. D. Stiles, "*Current-Driven Switching in a Single Exchange-Biased Ferromagnetic Layer*", Phys. Rev. Lett. **93**, 026601 (2004).

[124] A. Konovalenko, V. Korenivski, I. K. Yanson, and Y. G. Naidyuk, "*Spin-torque driven excitations and hysteresis in magnetic point contacts*", J. Appl. Phys. **99**, 08G503 (2006).

[125] I. K. Yanson, Y. G. Naidyuk, V. V. Fisun, A. Konovalenko, O. P. Balkashin, L. Y. Triputen, and V. Korenivski, "*Surface Spin-Valve Effect*", Nano Lett. **7**, 927–931 (2007).

[126] I. K. Yanson, V. V. Fisun, Y. G. Naidyuk, O. P. Balkashin, L. Y. Triputen, A. Konovalenko, and V. Korenivski, "*Current driven tri-stable resistance states in magnetic point contacts*", J. Phys.: Condens. Matter **21**, 355004 (2009).

[127] O. P. Balkashin, V. V. Fisun, I. K. Yanson, L. Y. Triputen, A. Konovalenko, and V. Korenivski, "*Spin dynamics in point contacts to single ferromagnetic films*", Phys. Rev. B **79**, 092419 (2009).

[128] I. K. Yanson, O. P. Balkashin, V. V. Fisun, Y. I. Yanson, and Y. G. Naidyuk, "*Current-field diagram for the magnetic states of a surface spin valve in a point contact with a single ferromagnetic film*", Low Temp. Phys. **39**, 279–284 (2013).

[129] S. Ingvarsson, G. Xiao, S. S. P. Parkin, and R. H. Koch, "*Tunable magnetization damping in transition metal ternary alloys*", Appl. Phys. Lett. **85**, 4995–4997 (2004).

[130] S. Ikeda, K. Miura, H. Yamamoto, K. Mizunuma, H. D. Gan, M. Endo, S. Kanai, J. Hayakawa, F. Matsukura, and H. Ohno, "*A perpendicular-anisotropy CoFeB-MgO magnetic tunnel junction*", Nature Mater. **9**, 721–724 (2010).

[131] A. Riegler, "Ferromagnetic resonance study of the Half-Heusler alloy NiMnSb", PhD thesis (Universität Würzburg, 2011).

[132] Y. Tserkovnyak, A. Brataas, and G. E. W. Bauer, "*Enhanced Gilbert Damping in Thin Ferromagnetic Films*", Phys. Rev. Lett. **88**, 117601 (2002).

[133] Y. Tserkovnyak, A. Brataas, and G. E. W. Bauer, "*Spin pumping and magnetization dynamics in metallic multilayers*", Phys. Rev. B **66**, 224403 (2002).

[134] Y. Sun, H. Chang, M. Kabatek, Y.-Y. Song, Z. Wang, M. Jantz, W. Schneider, M. Wu, E. Montoya, B. Kardasz, B. Heinrich, S. G. E. te Velthuis, H. Schultheiss, and A. Hoffmann, "*Damping in Yttrium Iron Garnet Nanoscale Films Capped by Platinum*", Phys. Rev. Lett. **111**, 106601 (2013).

[135] F. Wilhelm, P. Poulopoulos, G. Ceballos, H. Wende, K. Baberschke, P. Srivastava, D. Benea, H. Ebert, M. Angelakeris, N. K. Flevaris, D. Niarchos, A. Rogalev, and N. B. Brookes, "*Layer-Resolved Magnetic Moments in Ni/Pt Multilayers*", Phys. Rev. Lett. **85**, 413–416 (2000).

[136] P. K. Muduli, O. G. Heinonen, and J. Åkerman, "*Intrinsic frequency doubling in a magnetic tunnel junction-based spin torque oscillator*", J. Appl. Phys. **110**, 076102 (2011).

[137] A. Zholud and S. Urazhdin, "*Microwave generation by spin Hall nanooscillators with nanopatterned spin injector*", Appl. Phys. Lett. **105**, 112404 (2014).

[138] A. Giordano, M. Carpentieri, A. Laudani, G. Gubbiotti, B. Azzerboni, and G. Finocchio, "*Spin-Hall nano-oscillator: A micromagnetic study*", Appl. Phys. Lett. **105**, 042412 (2014).

[139] E. Iacocca, O. Heinonen, P. K. Muduli, and J. Åkerman, "*Generation linewidth of mode-hopping spin torque oscillators*", Phys. Rev. B **89**, 054402 (2014).

[140] E. Iacocca, P. Dürrenfeld, O. Heinonen, J. Åkerman, and R. K. Dumas, "*Mode-coupling mechanisms in nanocontact spin-torque oscillators*", Phys. Rev. B **91**, 104405 (2015).

[141] V. E. Demidov, H. Ulrichs, S. V. Gurevich, S. O. Demokritov, V. S. Tiberkevich, A. N. Slavin, A. Zholud, and S. Urazhdin, "*Synchronization of spin Hall nano-oscillators to external microwave signals*", Nat. Commun. **5**, 3179 (2014).

[142] M. R. Pufall, W. H. Rippard, S. E. Russek, S. Kaka, and J. A. Katine, "*Electrical Measurement of Spin-Wave Interactions of Proximate Spin Transfer Nanooscillators*", Phys. Rev. Lett. **97**, 087206 (2006).

[143] T. Kendziorczyk, S. O. Demokritov, and T. Kuhn, "*Spin-wave-mediated mutual synchronization of spin-torque nano-oscillators: A micromagnetic study of multistable phase locking*", Phys. Rev. B **90**, 054414 (2014).

[144] J. Grollier, V. Cros, and A. Fert, "*Synchronization of spin-transfer oscillators driven by stimulated microwave currents*", Phys. Rev. B **73**, 060409 (2006).

[145] B. Georges, J. Grollier, V. Cros, and A. Fert, "*Impact of the electrical connection of spin transfer nano-oscillators on their synchronization: an analytical study*", Appl. Phys. Lett. **92**, 232504 (2008).

[146] V. Tiberkevich, A. Slavin, E. Bankowski, and G. Gerhart, "*Phase-locking and frustration in an array of nonlinear spin-torque nano-oscillators*", Appl. Phys. Lett. **95**, 262505 (2009).

[147] E. Iacocca and J. Åkerman, "*Destabilization of serially connected spin-torque oscillators via non-Adlerian dynamics*", J. Appl. Phys. **110**, 103910 (2011).

[148] A. Khitun and K. L. Wang, "*Non-volatile magnonic logic circuits engineering*", J. Appl. Phys. **110**, 034306 (2011).

[149] F. Macià, A. D. Kent, and F. C. Hoppensteadt, "*Spin-wave interference patterns created by spin-torque nano-oscillators for memory and computation*", Nanotechnology **22**, 095301 (2011).

[150] S. Klingler, P. Pirro, T. Brächer, B. Leven, B. Hillebrands, and A. V. Chumak, "*Design of a spin-wave majority gate employing mode selection*", Appl. Phys. Lett. **105**, 152410 (2014).